

Investigations on the response of the
A4 calorimeter in the region of the
 $\Delta(1232)$ resonance using
Monte Carlo simulations

Diploma thesis by Luigi Capozza
born in Negrar, Italy

Institut für Kernphysik
Johannes Gutenberg-Universität Mainz
26th of October, 2004

Contents

1	Introduction	5
2	Parity violation in the excitation of the $\Delta(1232)$ resonance	7
3	The A4 experiment	11
3.1	Overview	11
3.1.1	The parity violation asymmetry	11
3.1.2	The experimental realization	14
3.2	ℓ -H ₂ Target and scattering chamber	16
3.3	Lead fluoride Cherenkov calorimeter	19
3.3.1	PbF ₂ crystals	21
3.3.2	Photomultipliers	23
3.4	Readout electronics of the lead fluoride calorimeter	25
4	Simulation of the detector response	29
4.1	Simulation of the deposition of energy in the PbF ₂ crystals using GEANT4	32
4.1.1	Geometry definition	32
4.1.2	Particles and physical processes	35
4.2	Production and detection of Cherenkov light	36
4.2.1	Producing and tracking optical photons	36
4.2.2	Detecting optical photons	39
4.3	Deposited energy vs number of photoelectrons	40
4.4	Digitization and histogramming	47
5	Simulation of physical processes	49
5.1	Kinematical region	49
5.2	Bremsstrahlung and straggling function	51
5.3	Elastic electron scattering off the proton	53
5.3.1	Unradiated cross section	53
5.3.2	Radiative corrections to elastic scattering	54
5.3.3	Sampling function	56
5.4	Inelastic electron scattering off the proton	57
5.5	Scattering off aluminium	60

6	Conclusions and outlook	61
6.1	Result of the simulation, comparison with the experimental energy spectrum	61
6.2	Outlook	64
A	Kinematics	67
B	Geometry details	71
	Bibliography	73

Chapter 1

Introduction

Within the A4 Collaboration an experimental apparatus for performing precise measurements of spin observables in the scattering of polarized electrons has been designed, developed and used during several years [1, 2, 3]. The experiment is realised at the MAMI electron accelerator facility. The polarized MAMI electron beam is scattered on an unpolarized liquid hydrogen target and the scattered electron are detected with a lead fluoride Cherenkov calorimeter.

So far, the measurements have been used for studying the elastic scattering of the polarized electrons off unpolarized protons [2, 3]. Nevertheless, the A4 experiment offers also the possibility to study the inelastic electron scattering off the proton. In fact, inelastically scattered electrons are detected during the measurements by the lead fluoride calorimeter together with the electrons scattered elastically. In particular, the A4 detector allows the detection of the electrons scattered exciting the $\Delta(1232)$ resonance, the lightest excited state of the proton. Therefore, the measurement of spin observables in the electroproduction of the $\Delta(1232)$ resonance is possible within the A4 experiment.

Scattering longitudinally polarized electrons on protons, the dependence of the scattering cross section on the helicity state of the electrons becomes observable and can be measured in terms of the asymmetry in the electron scattering cross section with the two helicity states of the electron, i.e. the parity violation asymmetry. It has been shown [4, 5, 6] that the parity violation asymmetry in the cross section for the electroexcitation of the $\Delta(1232)$ resonance can yield an important insight into the proton structure.

The scattering cross section asymmetry is obtained, in the A4 experiment, counting the number of electrons scattered with each state of helicity. The energy of the scattered electrons is measured by the lead fluoride calorimeter and histogrammed, giving an energy spectrum. Analysing this energy spectrum, it is possible to distinguish between electrons scattered elastically or inelastically, e.g. exciting the $\Delta(1232)$ resonance. Until now, the energy spectrum has been studied in detail only in the energy region of the elastic scattering, which was the subject of the measurements. For the analysis of the data in the energy

region of the $\Delta(1232)$ resonance excitation, a more detailed study of the energy spectrum is necessary for having a better knowledge of the background. In this energy range, a good understanding of the background is particularly essential because the ratio of the signal to the background is smaller than in the case of the elastic scattering range. This is because the absolute value of the signal cross section is smaller and because the background is larger.

The subject of this work is the detailed study of the lead fluoride detector response to the scattered electrons, in order to achieve a good comprehension of the electron energy spectrum in the energy region of the excitation of the $\Delta(1232)$ resonance. This is necessary for the further analysis of the data about the $\Delta(1232)$ resonance, in the perspective of the extraction of the parity violation asymmetry in the $\Delta(1232)$ electroproduction cross section.

For completeness, an overview of the physical motivation for measuring the parity violation in the electroexcitation of the $\Delta(1232)$ will be given in Chapter 2. Chapter 3 will provide a detailed description of the A4 experiment, concentrating above all on those features which are considered in the simulation of the detector response presented in Chapter 4. This simulation is used to compare the experimental energy spectrum with the physical cross sections for the electron scattering, which have been implemented within this work in an event generator, as reported in Chapter 5. The results of this comparison are exposed in Chapter 6, together with a short outlook on the further proceeding of the work.

Chapter 2

Parity violation in the excitation of the $\Delta(1232)$ resonance

Using a longitudinally polarized electron beam for performing electron-proton scattering experiments gives the possibility to study the helicity dependence of the electron-proton interaction. If such a dependence is observed, the symmetry of parity is violated in the process.

The observable associated with the helicity dependence is given by the asymmetry $A_{R/L}$ in the cross section of the electron scattering:

$$A_{R/L} = \frac{\sigma_R - \sigma_L}{\sigma_R + \sigma_L}, \quad (2.1)$$

with σ_R and σ_L representing the proton cross section for right-hand and left-hand polarized electrons, respectively.

The parity in the elastic electron-proton scattering is indeed violated, because the measurements of $A_{R/L}$ return values different from 0. For instance, within the A4 collaboration the quantity $A_{R/L}$ for the elastic electron scattering off the proton has been measured for determining the contribution of the strange sea quarks to the electromagnetic form factors of the nucleon [2]. Since the electromagnetic interaction is parity conserving, the observed parity violation can be understood, in the framework of the gauge theories of interacting quantum fields, considering the unified description of the electroweak interaction given by the Standard Model. Here, the effects of parity violation are expected in the processes involving weak neutral currents and arise at the lowest order from the interference of weak and electromagnetic amplitudes.

In the case of inelastic processes, the scattering of the electron is accompanied by the production of hadrons. In addition, one of the excited states of the proton can be produced. The lightest of such excited states is the $\Delta(1232)$ resonance, a spin- $\frac{3}{2}$ P -wave with isospin $\frac{3}{2}$. The cross section for the $\Delta(1232)$ electroproduction depends on the $p \rightarrow \Delta^+$ transition amplitude

$\langle \Delta^+ | J_\mu | p \rangle$, where the neutral current J_μ carries information related to the structure of the proton.

The excitation of the $\Delta(1232)$ resonance is an interesting process for several reasons. From the experimental point of view, the measurements are facilitated, because the excitation cross section is reasonably large and the $\Delta(1232)$ -state is energetically well isolated from the other heavier excited states of the proton. From the theoretical point of view, being $p \rightarrow \Delta^+$ a pure isovector transition, all isoscalar terms in J_μ are ruled out, simplifying the form of the transition amplitude and of the observables. Moreover, the only one strong decay channel allowed for the $\Delta(1232)$ is into a nucleon and a pion, i.e. $\Delta \rightarrow N\pi$, which enables one treating the unitarity issue quite rigorously.

Within the Standard Model, the current J_μ contains an electromagnetic term J_μ^γ and a weak term J_μ^Z . This last term makes the process of the $\Delta(1232)$ electroproduction helicity dependent, i.e. parity violating. Therefore, the observable $A_{R/L}^\Delta$ defined for this process like in Equation 2.1 is expected to be different from 0. $A_{R/L}^\Delta$ can be calculated in terms of J_μ and measured, in order to have an insight into the proton structure.

The first calculation of $A_{R/L}^\Delta$ was performed in 1978 by Cahn and Gilman [7]. They gave predictions for $A_{R/L}^\Delta$ within a variety of theoretical scenarios, namely assuming different gauge groups and assignments of fermion representations, treating the proton and the $\Delta(1232)$ with a constituent-quark-model. At that time, the Standard Model by Glashow, Salam and Weinberg was not yet well established and the main interest was focused on determining the coupling parameters of the weak gauge bosons to the various fermions of the theory. The measurement of $A_{R/L}^\Delta$ was seen as an opportunity for probing such aspects, rather than for studying the proton structure.

Few years afterwards, the result of the calculation of $A_{R/L}^\Delta$ considering the full spin- $\frac{3}{2}$ structure of the $\Delta(1232)$ as well as the dependence of J_μ on electromagnetic and weak structure functions was published by Nath, Schilcher and Kretzschmar [4]. It turned out that, at the born term level, $A_{R/L}^\Delta$ depends just on one weak structure function, which is associated with the axial vector coupling.

Nowadays, the coupling of leptons to the electroweak gauge fields is sufficiently well known, that electrons have become a very good tool for probing the hadron structure. Additionally, accelerator facilities with 100% duty factor and high polarized electron beams, e.g. MAMI, are these days operational. These machines allow the precise measurement of observables like $A_{R/L}^\Delta$.

Experimentally, it is only possible to measure $A_{R/L}^\Delta$ as the cross section asymmetry in the electron-proton inelastic scattering with the appropriate kinematics (see Appendix A). Contributions to this quantity are given both by resonant and non-resonant processes, without possibility to distinguish be-

tween them. Defining $A_{R/L}^{\Delta,\text{res}}$ and $A_{R/L}^{\Delta,\text{non-res}}$ as the resonant and non-resonant contributions to $A_{R/L}^{\Delta}$, respectively, this takes the form:

$$A_{R/L}^{\Delta} = A_{R/L}^{\Delta,\text{res}} + A_{R/L}^{\Delta,\text{non-res}}. \quad (2.2)$$

According to [6], defining G_F as the Fermi constant, α as the electromagnetic fine structure constant, Q^2 as the absolute value of the squared four momentum transfer and s as the square of the total energy in the centre of mass frame, $A_{R/L}^{\Delta,\text{res}}$ can be written as:

$$A_{R/L}^{\Delta,\text{res}} = \frac{-G_F}{\sqrt{2}} \frac{Q^2}{4\pi\alpha} [g_A^e \xi_V^{T=1} + g_V^e \xi_A^{T=1} F(Q^2, s)], \quad (2.3)$$

where g_A^e and g_V^e are the axial vector and the vector electron coupling to the Z^0 field, respectively. The isovector hadron- Z^0 couplings are denoted with $\xi_V^{T=1}$ and $\xi_A^{T=1}$ for the vector and axial vector current, respectively. These factors are, at the tree level in the Standard Model and being θ_W the weak mixing angle:

$$\begin{aligned} g_A^e &= 1, \\ g_V^e &= -1 + 4 \sin^2 \theta_W, \\ \xi_V^{T=1} &= 2(1 - 2 \sin^2 \theta_W), \\ \xi_A^{T=1} &= -2. \end{aligned}$$

The factor $F(Q^2, s)$ is the structure function, which brings the interesting information about the baryon physics. The theoretical importance in the chiral perturbation framework of the measurement of $F(Q^2, s)$ and the theoretical difficulties for analysing such a measurement are discussed in [6].

The background non-resonant contribution $A_{R/L}^{\Delta,\text{non-res}}$ to the asymmetry has been so far estimated at the Born term level within a phenomenological model with effective Lagrangians [5]. The model dependence introduces a theoretical uncertainty for the extraction of the resonant contribution $A_{R/L}^{\Delta,\text{res}}$ from the observable $A_{R/L}^{\Delta}$. In the same work [5], also a prediction for the resonant part $A_{R/L}^{\Delta,\text{res}}$ of the asymmetry is given in the Born approximation, with effective Lagrangians and phenomenological $p\Delta$ transition currents.

Besides the study of hadron structure, the measurement of $A_{R/L}^{\Delta}$ could be interesting also for other aspects. Supposing that the proton structure were ‘‘sufficiently’’ well known, the attention could be set back onto the Standard Model and the measurement of $A_{R/L}^{\Delta}$ could yield more general information about the theory of the electroweak interaction beyond the Standard Model. Such possibility has been investigated, e.g. in [6]. In that work two examples of how the Standard Model could be impacted are given, namely the modification of the form of the gauge boson propagators by radiative corrections and the introduction of the tree-level exchange of new, heavy particles.

Chapter 3

The A4 experiment

The scope of this chapter is a description of the A4 experiment at the MAMI facility. It will focus particularly on those aspects which are most relevant for the further discussion about the detector response simulation.

3.1 Overview

3.1.1 The parity violation asymmetry

The principle of the parity violation experiment of the A4 Collaboration is shown schematically in Figure 3.1. A longitudinally polarized electron beam is scattered by an unpolarized liquid hydrogen target. An electromagnetic calorimeter detects the scattered particles and measures their energies. These particle energies are digitized and histogrammed giving an energy spectrum like in Figure 3.2. The peak appearing on the right in the histogram of Figure 3.2 corresponds to the elastically scattered electrons. Moving toward the left side one encounters the energy region corresponding to the inelastic scattering, i.e. hadrons are produced in the scattering. About in the middle between the left end of the picture and the elastic region, the peak corresponding to the exci-

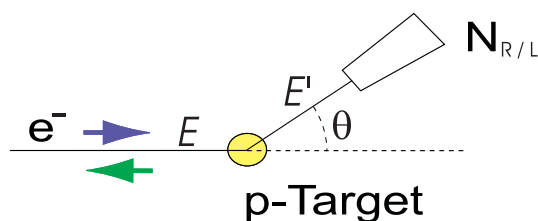


Figure 3.1: Principle of the A4 experiment. Polarized electrons scatter with energy E off unpolarized protons with a scattering angle θ . They are detected by an electromagnetic calorimeter and their final energy E' is measured.

tation of the $\Delta(1232)$ resonance is visible. At the very left side, the large low energy background signal is shown.

For subdividing more precisely the energy spectrum into ranges, according to the nature of the scattering process in which the electron has been produced, e.g. elastic scattering, inelastic scattering, excitation of the $\Delta(1232)$, one needs to know the kinematics of the scattering process. Knowing both the energy of an electron entering the calorimeter and the polar angle θ like shown in Figure 3.1, it is possible to determine this kinematics (see Appendix A). For instance, electrons with the initial beam energy $E = 854$ MeV and scattered at $\theta = 35^\circ$ with final energy $E' = 734$ MeV have scattered elastically, while electrons with the same initial energy and scattering angle but with final energy $E' = 442$ MeV have transferred to proton the exact amount of energy for exciting the $\Delta(1232)$ resonance with maximal probability. Following this kind of reasoning, the vertical lines in Figure 3.2 mark the energy values corresponding to the kinematics of elastic scattering, pion production threshold and maximum of the $\Delta(1232)$ resonance excitation peak. Moreover, these vertical lines subdivide the spectrum into energy regions corresponding to different processes by fixing three “cuts”. These, together with the pion production threshold, determine the intervals of integration for counting the elastically scattered electrons (in gray in Figure 3.2) and the electrons scattered in the kinematical region corresponding to the excitation of the $\Delta(1232)$ resonance (in green in Figure 3.2). These “cuts for the $\Delta(1232)$ resonance” are not univocal, because they have to be fixed in the analysis according to the theoretical calculation chosen for comparison. In these calculations an integration interval for the $\Delta(1232)$ resonance has also to be decided.

Integrating the energy spectrum between the two elastic cuts (Figure 3.2), one obtains the number of elastically scattered electrons N_R^{el} and N_L^{el} for the two states of electron polarization R and L , respectively. The difference between N_R^{el} and N_L^{el} divided by their sum gives the observable $A_{R/L}^{el}$:

$$A_{R/L}^{el} = \frac{N_R^{el} - N_L^{el}}{N_R^{el} + N_L^{el}}. \quad (3.1)$$

This quantity is the parity violation asymmetry (PV asymmetry) in the cross section for the elastic scattering of polarized electrons off unpolarized protons. In the same way it is possible to integrate the electron energy spectrum over the energy interval corresponding to the excitation of the $\Delta(1232)$, for the two states of polarization R and L . This gives the number of electrons N_R^Δ and N_L^Δ , respectively, which have excited the proton to the $\Delta(1232)$ state. Using N_R^Δ and N_L^Δ to build the PV asymmetry $A_{R/L}^\Delta$ in the cross section for the excitation of the $\Delta(1232)$, one can write:

$$A_{R/L}^\Delta = \frac{N_R^\Delta - N_L^\Delta}{N_R^\Delta + N_L^\Delta}. \quad (3.2)$$

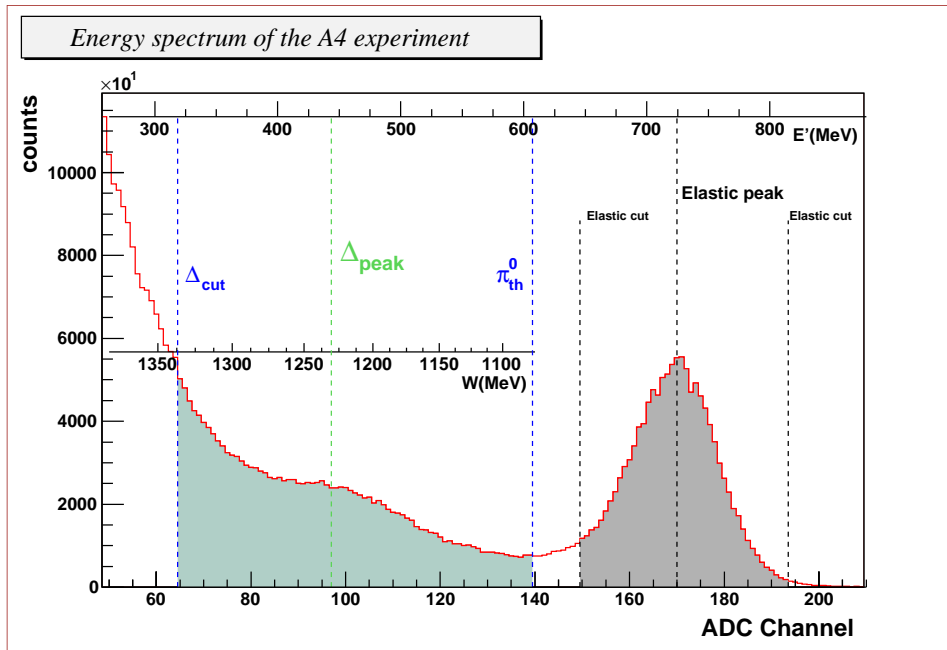


Figure 3.2: Example of an energy spectrum of 854.3 MeV longitudinally polarized electrons scattered off unpolarized protons, as measured by the A4 lead fluoride Cherenkov calorimeter. The bottom x-axis shows the digitized value of the measured energy in ADC channels. The axis on top of the picture shows the corresponding value in MeV of the final energy E' of a scattered electron. The third axis in the middle (W) shows the corresponding mass of the excited hadronic state for electrons scattered at $\theta = 35^\circ$ (see Appendix A for details). The filled regions are integration intervals for the $\Delta(1232)$ (in green) and for the elastic events (in grey). The vertical lines indicate the position of the $\Delta(1232)$ peak (green), of the π^0 threshold and a possible $\Delta(1232)$ region lower cut (blue), of the elastic peak and the elastic cuts (black).

The measurement of this observable gives an insight into the proton structure like described in Chapter 2.

3.1.2 The experimental realization

The details about the concept of the A4 experiment are shown schematically in Figure 3.3.

The continuous polarized electron beam is produced at the MAMI facility with a current I of $20 \mu\text{A}$ and a polarization P of about 80%. The electron source is a strained layer of GaAs. This crystal is used as a photocathode which is irradiated with light pulses of 100 ps of duration. The pulses are produced by an optical semiconductor laser system emitting a circularly polarized light. The helicity of this circularly polarized light determines the helicity of the beam electrons and is changed by a Pockel cell. The photoelectrons emitted at the GaAs crystal by photoelectric effect are injected into the MAMI accelerator after being extracted by a high voltage potential of 100 kV. The MAMI accelerator consists of an injector, a linear accelerator of an energy of 3.46 MeV, and of three racetrack microtrons (RTM). These accelerate the electrons up to an energy of respectively 14.35 MeV, 180 MeV and 854.3 MeV, which is the beam energy used by the A4 experiment. The maximal energy of the MAMI facility is 882 MeV but the energy used in the A4 experiment is 854.3 MeV, in order to have the right spin orientation, considering the spin precession along the beam transport line from the accelerator to the experimental hall.

The beam parameters, namely current, energy, position and angle respect to the mean direction, present fluctuations, which affect the number of electrons scattered in the target and detected by the lead fluoride calorimeter per time unit. These fluctuations can be either helicity uncorrelated or helicity correlated, meaning that they do not depend on the change of the beam polarization or that they do depend on it, respectively. The helicity uncorrelated fluctuations in the beam parameters just increase the noise in the measurement, while the helicity correlated fluctuations arise false asymmetries, which have to be subtracted from the raw asymmetry. For this reason, it is of major importance that the beam parameters be strictly under control. Hence several stabilization systems, for reducing the fluctuations in the beam parameters in general, and monitoring systems, for having the possibility of subtracting the false asymmetries due to helicity correlated fluctuations, are employed. Such systems are located both at the accelerator, along the beam transport line, and in the A4 experimental hall.

The polarization P of the beam must be known since it gives the ratio be-

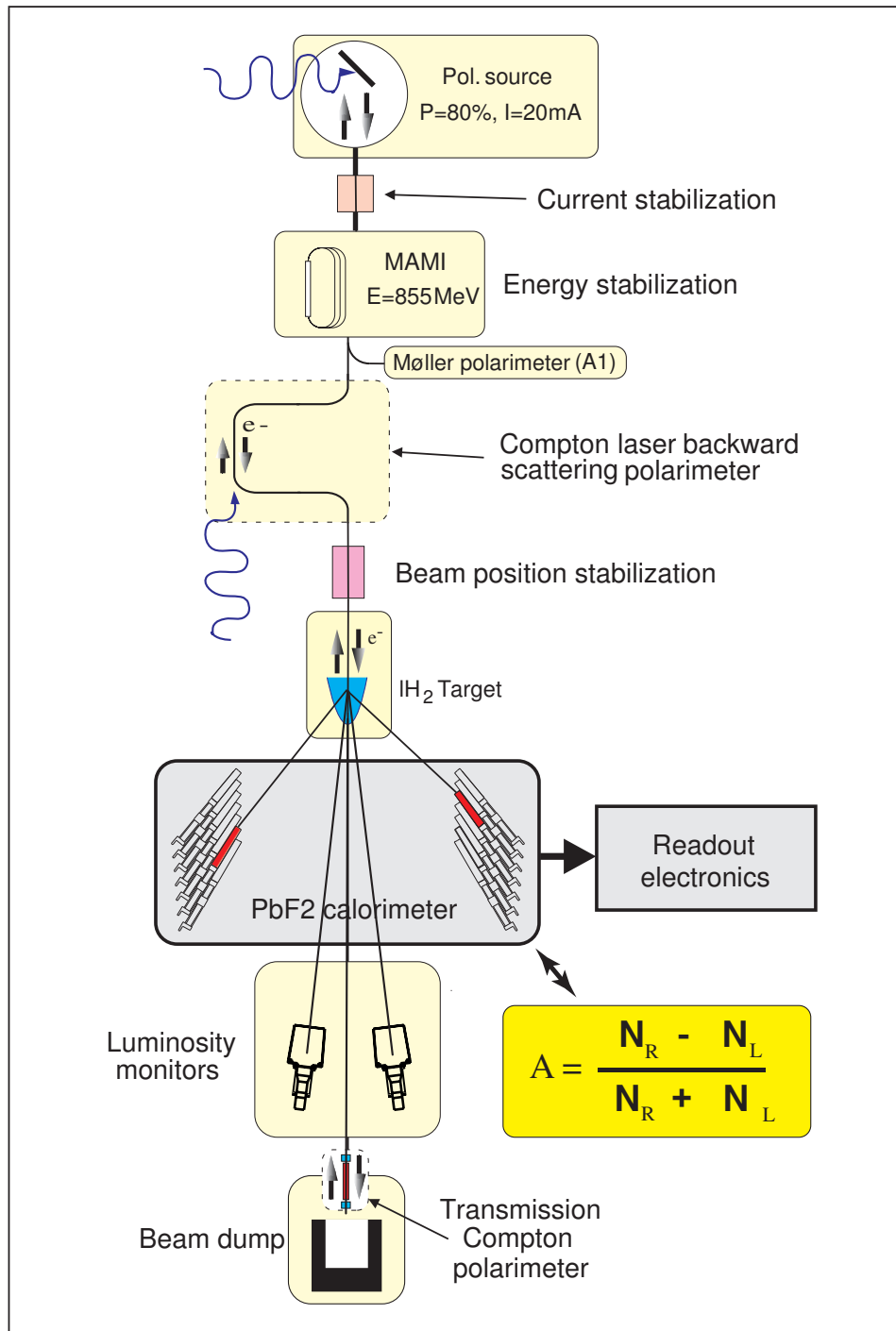


Figure 3.3: Details of the experimental concept.

tween the physical PV asymmetry A_{phys} and the measured asymmetry A_{meas} :

$$A_{phys} = PA_{meas}. \quad (3.3)$$

To measure P a Møller polarimeter located before the A4 hall is used for an absolute measurement. Furthermore a backward scattering Compton polarimeter is being built in the experimental hall just before the target. This will provide a run time non-destructive absolute measurement of P [8, 9]. Presently, together with the Møller polarimeter, a transmission Compton polarimeter placed before the beam dump [10] is used for relative measurements, which provide a non-destructive run time monitoring of P .

The most important parts of the experimental setup, concerning this work, are the target, the scattering chamber, the lead fluoride Cherenkov calorimeter and its readout electronics. These are described in much detail in the next sections of this chapter.

Concluding with the description of the experimental concept, the target density has to be monitored, because its fluctuations are source of additional noise. This is done by means of the luminosity monitors, which are placed behind the target, at the end of the scattering chamber [11].

In Chapter 4 a detailed simulation of the response of the experimental apparatus to the electrons scattered in the target is presented. The simulation deals with the passage of the scattered electrons through the materials located on the path from target to detector and with the detection of these electrons by the lead fluoride calorimeter. Hence it is here worth reporting the details of the experimental setup, which are taken into account in the simulation described in Chapter 4. Section 3.2 presents the geometrical specifications of target and scattering chamber. In Section 3.3 details about the geometry of the electromagnetic calorimeter, about the Cherenkov material lead fluoride and about the photomultiplier tubes are given. Finally Section 3.4 concentrates on the features of the readout electronics.

3.2 ℓ -H₂ Target and scattering chamber

The target consists of an aluminium cell containing liquid hydrogen (see Figure 3.4). It is situated inside a vacuum scattering chamber like shown in Figure 3.5. The beam electrons scattered off the protons of the liquid hydrogen leave the target travelling through the liquid hydrogen itself and through the aluminium wall of the target cell. For reaching the lead fluoride detector they have to pass through the vacuum inside the scattering chamber, through the aluminium wall of the same scattering chamber and through the air layer between scattering chamber and calorimeter.

All this layers of material lying on the path of the scattered electrons from

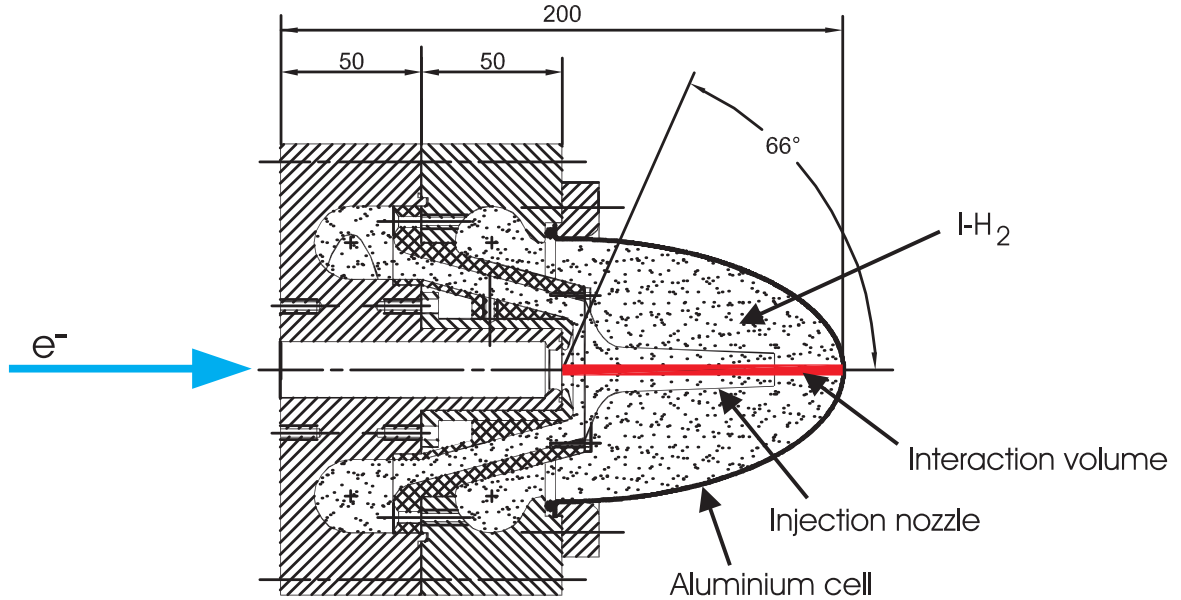


Figure 3.4: Side view of the liquid hydrogen target (dimensions in mm).

target to detector are considered in the simulation described in Chapter 4. Therefore, in this section, the geometrical details of the liquid hydrogen target and of the scattering chamber are presented.

ℓ -H₂ Target. The shape of the target cell is a paraboloid of 100 mm of length (see Figure 3.4). The aluminium wall thickness is about 250 μm . The incoming window is an aluminium foil of 50 μm of thickness. The total length of the hydrogen layer is 95 mm. The liquid hydrogen is injected into the target cell through an aluminium nozzle, having a thickness of 200 μm , a diameter of 20 mm and a length of 70 mm.

With the configuration shown by Figure 3.4, the electrons that are scattered with polar angle between 0° and 66° can leave the target passing through at most about $1.5 \cdot 10^{-2}$ radiation lengths of materials. This is important since the luminosity monitors cover a polar angle between 4.4° and 10° , while the lead fluoride calorimeter covers the polar angle interval from 30° to 40° .

The hydrogen is kept at a temperature of 14 K by a helium heat exchanger. The helium temperature is monitored and controlled electronically. This way the hydrogen temperature is stabilized just above the freezing point and well distant from the boiling point.

The mean density of the hydrogen inside the target is $7.08 \cdot 10^{-2} \text{ g/cm}^3$

Vacuum scattering chamber. Figure 3.5 shows a schematic side view of the vacuum scattering chamber and of the lead fluoride calorimeter. The scattering chamber is an aluminium tube positioned with the symmetry axis

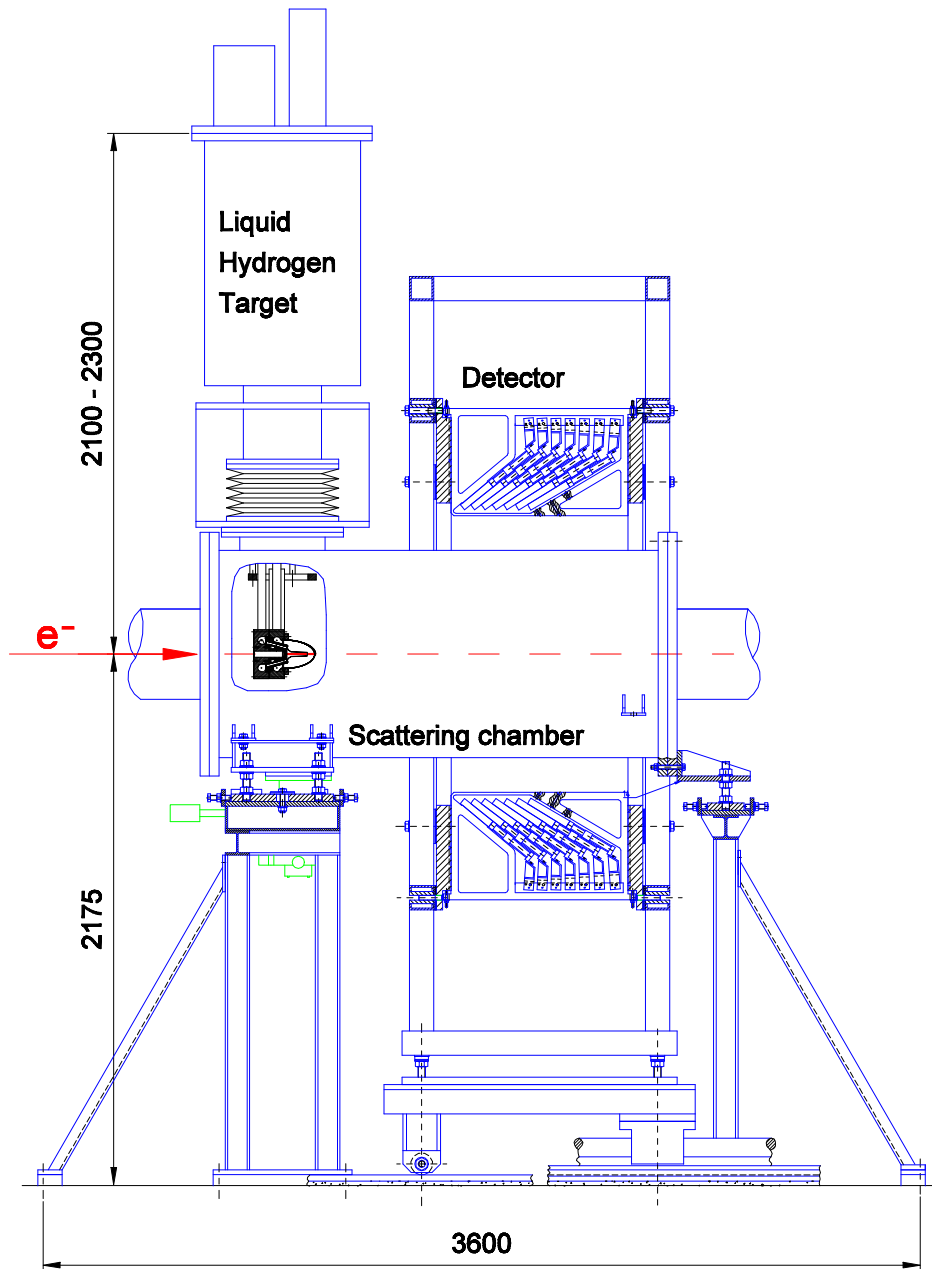


Figure 3.5: Side view of the vacuum scattering chamber (dimensions in mm).

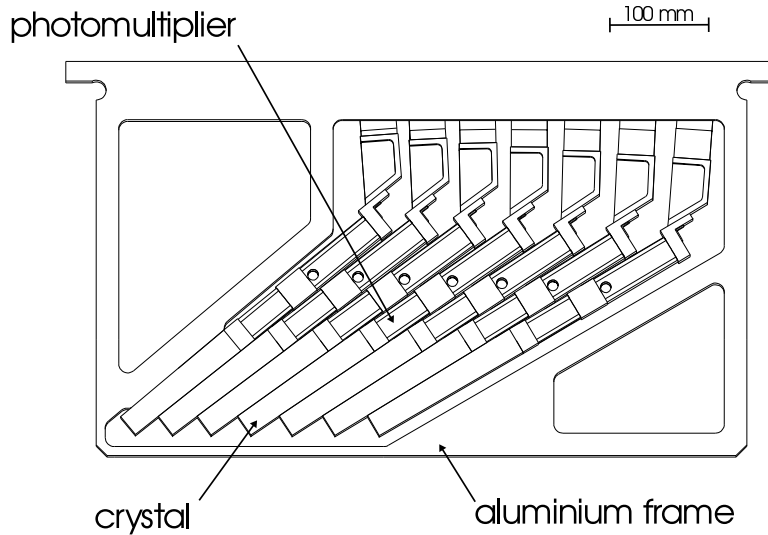


Figure 3.6: Schematic view of one frame supporting 7 crystals with their photomultipliers. The beam propagation direction is from the left to the right and the beam line lies below the bottom of the picture. The symmetry axes of the crystals point to the bottom left side toward the target.

lying on the beam line. It is flange-mounted to the beam pipe at one extremity and to the exit beam line at the other (in Figure 3.5 on the left and on the right side, respectively). The dimensions are 190 cm of length, 85 cm of external diameter and 25 mm of thickness. The thickness is reduced to 5 mm in the central part of the chamber (75 cm long), which lies right on the path between target and detector, i.e. the particles coming out of the target and being detected in the calorimeter must pass through a thinner layer of aluminium.

The pressure inside the chamber amounts to a few nanobar, this assures that the straggling effect on particles due to the passage through the chamber is completely negligible.

3.3 Lead fluoride Cherenkov calorimeter

The detector of the A4 experiment is a homogeneous electromagnetic shower calorimeter using the Cherenkov radiator lead fluoride (PbF_2) as active material. Since no scintillation is present in the PbF_2 and the duration of the Cherenkov light pulses is very short, the detection of particles at very high rate is possible. The detector covers the scattering polar angle θ between 30° and 40° and the whole 2π range of azimuthal angle ϕ . The total solid angle Ω covered by the detector amounts to 0.63 sr. The calorimeter contains 1022 PbF_2 crystals, organized in 7 rings and mounted on 146 frames.

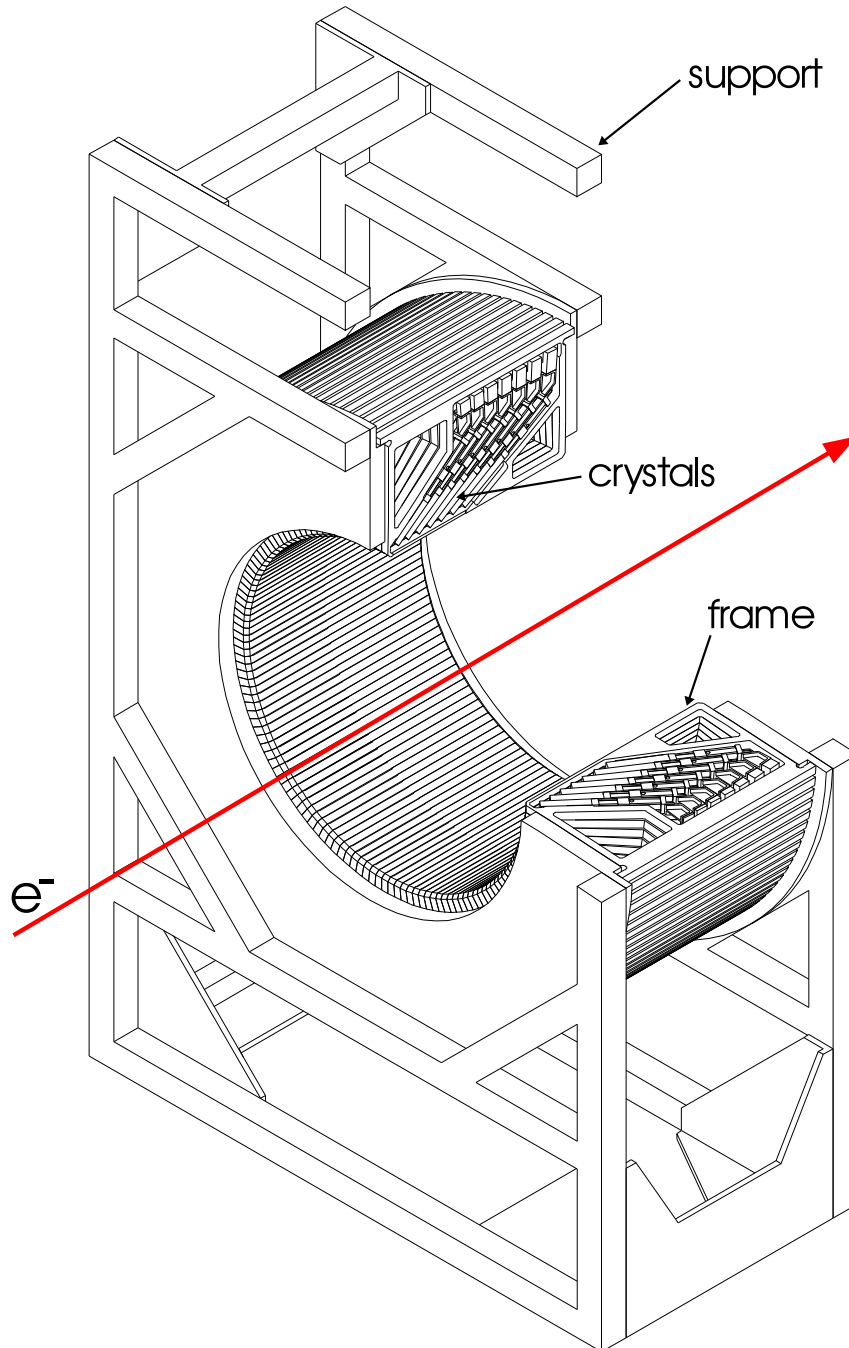


Figure 3.7: Schematic view of the lead fluoride Cherenkov calorimeter. In this picture one quarter of the detector has been cut to permit the view of the crystals and their supporting frames. The red arrow indicates the beam line and the beam direction.

At the end of each crystal a photomultiplier tube is mounted to detect the Cherenkov light produced inside the lead fluoride. The crystals and their photomultipliers are mounted on aluminium frames like shown in Figure 3.6. Each frame contains 7 trapezoidal prism shaped crystals. These are positioned with different orientation and have different dimensions.

The orientation is such that the axis of each prism passes through the centre of the target, that is the parallel faces of the prisms focus on the target. This way the electrons scattered into the solid angle covered by the detector with different polar angle θ move always almost perpendicularly to the surface of one crystal. More details on the dimensions and positions of the crystals are given in Appendix B.

The detector contains 146 of these frames (1022 crystals) mounted on an aluminium support like shown in Figure 3.7. It has a ring shape, i.e. it is cylindrical symmetric (ϕ -symmetric) and has a central cavity (Figure 3.7). It is mounted on an aluminium support so that the scattering chamber can be inserted into the ring-hole and the symmetry axis lies on the beam line (Figure 3.5).

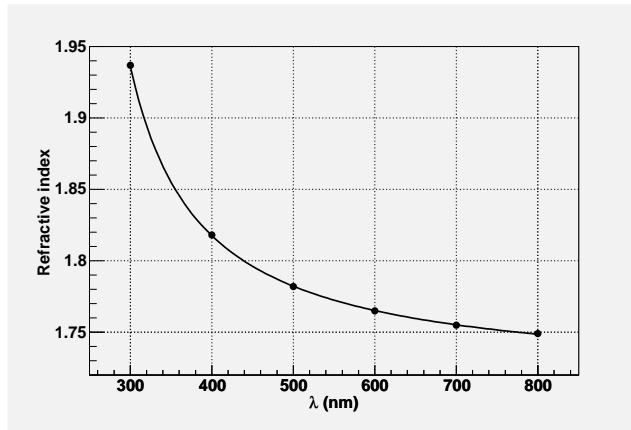
With this configuration, the crystals form 7 rings each covering a different solid angle $\delta\Omega_i = \Delta\phi\delta\theta_i \sin\theta_i$ ($i = 1, \dots, 7$), where $\Delta\phi = 2\pi$ for all rings, while θ_i and $\delta\theta_i$ depend on the ring number i (see Appendix B). Conventionally the numbering of the rings increases with decreasing polar angle θ . Altogether the θ -interval covered by the whole detector is from 30° to 40° .

The inner, target side of the aluminium frames (lower side in Figure 3.6) constitutes a layer of material lying on the path of particles getting from the target into the detector. The thickness of this layer is 10 mm.

3.3.1 PbF₂ crystals

Beside the geometrical features of the experimental setup, the physical characteristics of the materials constituting the various parts of the apparatus are needed for the simulation presented in Chapter 4. In particular, the formation of electromagnetic cascades and the emission of Cherenkov radiation in lead fluoride by the electrons scattered in the target and detected by the calorimeter are treated in the simulation. The characteristic of lead fluoride are at most relevant for the presented simulation and, thus, listed in the following.

Lead Fluoride (PbF₂) is a transparent salt with cubic crystalline structure. It has a density ρ of 7.77g/cm³, a radiation length X_0 of 0.93 cm, a Molière radius R_M of 2.2 cm, a critical energy E_c of 9.04 MeV, a refractive index larger than 1.7 for visible wavelengths (1.8 at 400 nm, see Figure 3.8) and an optical cutoff at about 280 nm. Its radiation resistance and radiation induced absorption bands were investigated [13] and optical bleaching of crystals was



$$\text{Fit function: } n(\lambda) = a_0 \cdot \exp\left(\frac{a_1}{\lambda - a_2}\right);$$

$$a_0 = 1.7167, \quad a_1 = 10.87, \quad a_2 = -209.78.$$

Figure 3.8: Refractive index n of PbF_2 as a function of the wavelength λ . The data points and the phenomenological fit function were taken from Grimm [12].

found to be possible and effective.

Furthermore no scintillation component was found in the light output of lead fluoride [14]. Being this light pure Cherenkov radiation due to the passage of particles, the duration of the signal pulse in photomultipliers in response to an incoming particle is very short ($< 20ns$). This allows high rate particle detection, which is a stringent requirement of the A4 experiment.

All these features make lead fluoride a good material for electromagnetic calorimetry. The energy resolution was measured to be of the order [13]

$$\frac{\Delta E'}{E'} = \frac{3.2\%}{\sqrt{E'/GeV}}, \quad (3.4)$$

which allows precise energy measurements. In Equation 3.4 the measured energy is denoted with E' to be consistent with the definitions of the kinematical quantities given in Appendix A.

In order to obtain a better yield of the light through the crystals into the photomultipliers, the crystals were wrapped with reflective foils. The chosen material is *Immobilon-P*. The thickness of the foils is about $120 \mu\text{m}$. The reflectivity for photon wavelengths greater than 280 nm is almost independent from the wavelength and has a mean value of about 95%, as one can see from Figure 2.32 of [15]. This information is also needed by the simulation, as explained in Chapter 4, because the transmission of the Cherenkov photons

through the PbF_2 crystals is also simulated.

3.3.2 Photomultipliers

Like the production of Cherenkov photons and their propagation through the PbF_2 crystals, also their detection by the photomultiplier tubes is taken into account in the simulation presented in this work. The characteristic of the photomultipliers, which enters into the simulation, is their quantum efficiency. This section is dedicated to define this quantity and to give the corresponding value for the photomultiplier tubes (PMT's) used in the A4 experiment.

The response of photomultipliers to incident light is determined mostly by the input window material and the photocathode material.

The transmission coefficient T of the input window material determines the light spectrum which is able to hit the photocathode. It is the ratio of the transmitted power to the incident power and it depends on the wavelength λ . The function $T(\lambda)$ is about constant for wavelengths longer than a certain *cut-off wavelength* λ_c and, for λ shorter than λ_c , it drops down to 0 with decreasing λ . The plateau value of $T(\lambda)$ is typically about 90%. The cut-off wavelength is defined as that wavelength where the transmission coefficient assumes a value $T(\lambda_c)$ which is 10% less than the plateau value.

The photocathode material is characterized by a sensitivity to the incident light. This is not defined independently from the transmission through the input window. It is studied by means of the response of the whole photomultiplier, which is given for instance by the quantum efficiency.

The *quantum efficiency* QE is defined as the ratio of the number of photoelectrons emitted by the photocathode to the number of photons incident on the window, and is usually expressed as a percentage. It depends on the wavelength of the photons and is generally less than 35%.

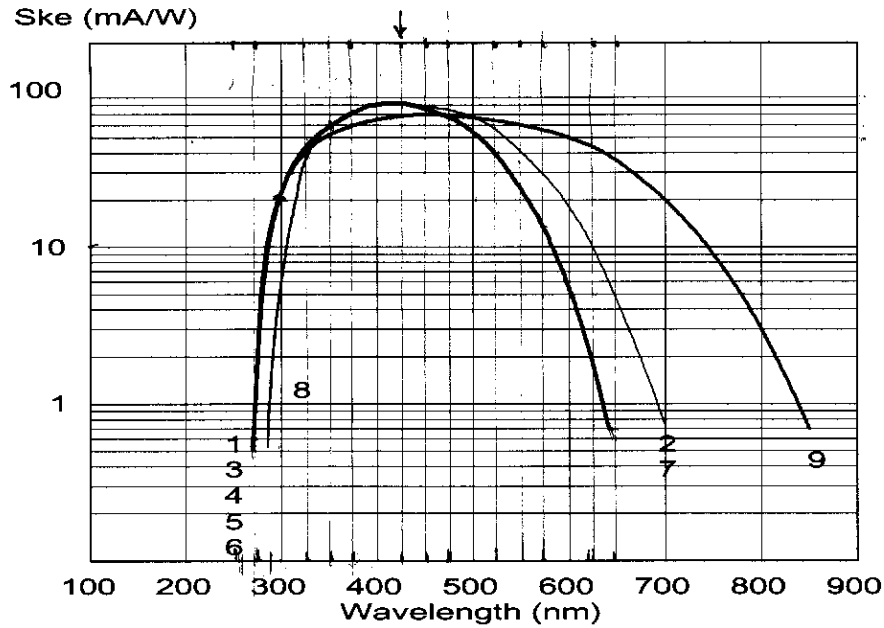
Because it is easier to measure the photocathode current produced in response to an incident light power than to count photons and electron, the photoemission is frequently described by the cathode *radiant sensitivity* $sk_e(\lambda)$. This is defined as the current measured at the photocathode over the incident light power at a given wavelength λ and is usually expressed in mA/W.

Cathode radiant sensitivity and quantum efficiency are related to each other by the empirical expression:

$$QE \simeq \left(\frac{124 \cdot \text{nm}}{\lambda} \times sk_e \cdot \frac{\text{W}}{\text{mA}} \right) \% . \quad (3.5)$$

The graph of the function $sk_e(\lambda)$ is called *spectral sensitivity characteristic* (Figure 3.9) and represents the spectral response of the photomultiplier. This is determined at the longer wavelengths by the thickness and the photoemission

TYPICAL SPECTRAL CHARACTERISTICS



This graph was taken from [16] and shows the spectral response of different kind of tubes produced by *Photonis*. Curve 1 corresponds to the XP2900. The window material is lime glass for PMT's 7 and 8, borosilicate for all other tubes. The photocathode material is a multialkali antimonide (SbNa_2KCs) for Curve 9, a green-extended bialkali antimonide (GEBA) for 2 and 7 and the bialkali antimonide SbKCs for the rest. A summary is given in the following table:

curve no.	tube type	photocathode material	window material
1	XP2900	bialkali	borosilicate
2	XP2901	GEBA	borosilicate
3	XP2910	bialkali	borosilicate
4	XP2920	bialkali	borosilicate
5	XP2930	bialkali	borosilicate
6	XP2960	bialkali	borosilicate
7	XP2961	GEBA	lime glass
8	XP2962	bialkali	lime glass
9	XP2963	multialkali	borosilicate

Figure 3.9: Spectral sensitivity characteristic of some Photomultipliers.

threshold of the photocathode. At the shorter wavelengths the input window transmission becomes the determining factor.

The photomultiplier tubes used in the A4 calorimeter are of the type XP2900, produced by *Photonis* [16]. They are 98 mm long and they have an external diameter of 28.5 mm. The diameter of the photocathode is 24 mm. The input window material is a borosilicate glass. This has a cut-off wavelength of 270 nm. The photocathode material is the bialkali antimonide SbKCs. The spectral sensitivity characteristic is shown in Figure 3.9.

3.4 Readout electronics of the lead fluoride calorimeter

One last experimental specification has to be described here, since it is considered in the simulation (see Chapter 4). It is the functionality of the readout electronics of the Cherenkov detector.

Given the photomultipliers signal as input, the readout electronics has to deal with three main tasks.

1. It identifies the signal of a scattered electron and assigns it to a channel (crystal).
2. It measures the energy of the electron, digitizes and histograms that value.
3. It detects multiple hits events (pile-up) in order to inhibit their registration.

1. Identification of events. Within the electromagnetic cascade generated in the PbF_2 crystals by one high energy electron getting into the detector, many relativistic charged particles are produced. The passage of these particles through the crystals generates a Cherenkov light pulse, which induces some current pulse signals in the photomultiplier tubes. When the signal of one PMT becomes greater than a certain threshold, a pulse shaper is used to check if a pulse occurs and consequently to identify one event.

Considering that the Molière radius R_M of PbF_2 is 2.2 cm and considering the energies of the electrons to be detected, the dimensions of the crystals (see Appendix B) were decided in such a way that more than 95% of one electromagnetic cascade is expected, on average, to develop inside a cluster of 9 crystals, that is a 3×3 matrix like shown in Figure 3.10 by channels 0 to

8. Therefore, when one event is identified, more than one neighbouring PMT gives a pulse simultaneously and the event must be assigned to one of these channels. This selected channel corresponds to the crystal where the largest energy deposition occurred and will be called *local maximum*. The event is assigned to this channel because, on average, the impact position of the detected electron with the lead fluoride lies on the surface of the crystal where the largest energy deposition occurs. The energy the charged particles of the cascade deposit in the crystals happens to be proportional to the number of Cherenkov photons produced and detected. This is discussed in more details in Section 4.3. Moreover the current signal of the PMT's has an intensity proportional to the number of photoelectrons emitted by the photocathode per time unit. The channel assignment is obtained comparing the PMT signals with those of the neighbouring PMT's and selecting the stronger one. The comparison is carried out between two "direct" neighbours. For instance the signal of channel 0 in Figure 3.10 is compared with those of channels 1, 3, 5 and 7. If it turns out to be stronger than every one of them, channel 0 is recognized as a local maximum and the event is assigned to it.

2. Energy Measurement. The electrons getting into the detector deposit almost all of their energy in the crystals by generating electromagnetic showers. Therefore the deposited energy is a measurement of the incoming electron energy. On the other hand, measuring the deposited energy is equivalent to counting the number of detected photoelectrons during the Cherenkov light pulse induced by the cascade, like will be discussed in Section 4.3. Such a counting is achieved by integrating the current pulse signals of the PMT's over time and summing the obtained charge values over the channels of interest.

Two aspects have to be taken into account by performing such integration and summation. These are the duration of the cascade and its spatial dimensions. Integrating the current signal over time implies fixing a time integration window τ . This must be long enough to include the whole shower development, though not too long in order to avoid temporal pile-up. The time window which happens to be optimal is $\tau=20$ ns. The electromagnetic shower is expected to develop for more than 95%, on average, within a cluster of 9 crystals, that is the 3×3 matrix of crystals centred on the local maximum channel like shown by channels 0 to 8 in Figure 3.10. Therefore, the summation of the charge values for having the total charge of an event is done over these nine channels.

The charge value obtained after integration and summation is compared with a given threshold. If the value is greater than the threshold, it is digitized and registered in a histogram. The histogram contains 256 bins and the offset is typically some negative value, that is a charge value equal to 0 corresponds to a bin smaller than 0 (physical 0). Due to small production

ring 1														
ring 2		R7	R6	R5	R4	R3								
ring 3		R8	4	3	2	R2								
ring 4		R9	5	0	1	R1								
ring 5		R10	6	7	8	R16								
ring 6		R11	R12	R13	R14	R15								
ring 7														

Figure 3.10: Representation of the readout scheme of the detector. Each square cell represents a channel. The rows correspond to the 7 rings and the columns represent the frames. In the whole detector these would be 146. Red cells represent local maxima and yellow cells the neighbouring channels which contribute to the summation in one event (see text). The blue cells R1 to R16 contribute to the logical veto for rejecting spatial pile-up events.

differences in the electronic components the sensitivity is slightly different for different electronic channels. In the calibration of the lead fluoride detector, these differences have been measured and are taken into account for calculating the charge corresponding to the position of the elastic peak (Figure 3.2). In order to compare the results of the simulation presented in this work with the experiment, a recalculation of the PMT charge values from the measured ADC values is necessary.

3. Detection of multiple hits events (pile-up). Two kinds of pile-up events have to be considered. *Temporal pile-up* occurs when two different particles with sufficient energy contribute to the current signal of the same channel during the integration time τ . To recognize such events a pulse shaper is activated during the 20 ns of time integration window τ for finding temporal maxima in the current signal. In a single hit event, the pulse shape develops during the first 5 ns of the time window τ . If any further pulse is detected in the following 15 ns, the event is recognized as temporal pile-up and a veto digit inhibits its registration. If no further pulses are detected in those 15 ns,

the event is registered.

Spatial pile-up is given when two particles hit the detector close to each other during the time window τ . To detect this situation the electronics looks for local maxima at the end of each integration time. If it finds more than one local maximum within a 5×5 matrix of crystals the spatial pile-up veto is enabled and the event is not considered for histogramming. Such a matrix is represented on the left in Figure 3.10 on the left by crystals 0 to 8 and $R1$ to $R16$. On the right in the same Figure an example of spatial pile up is given.

Chapter 4

Simulation of the detector response

In this chapter a simulation of the response of the A4 experimental apparatus to the electrons scattered inside the liquid hydrogen target is presented. First some terms important to the further discussion must be defined. Then the general strategy of the simulation will be traced, delineating the main issues and how they have been addressed in this work.

In the following a simplified description of what happens in the experiment, that is of what has to be simulated, is drawn in order to define some useful terms for the discussion in this chapter.

Inside the target several reactions take place because of the incident beam. In general the final states of these reactions are particles of a certain species, which are in a certain position and have a certain momentum. One set containing these three pieces of information will be referred to as *event* and the particle of one event will be called *primary particle* or *primary*. The primary particles undergo possibly other interaction processes with the material on their path, so that their momentum is modified and more particles, *secondary particles* or *secondaries*, are created.

A certain number of particles, primaries or secondaries, reaches the detector, where further interactions occur, namely electromagnetic cascades and Cherenkov radiation, and further secondaries are created. Among these particles, the Cherenkov optical photons are the ones which are detected by photomultipliers, i.e. they let the photomultipliers produce some signal. This signal is then digitized and histogrammed to give the energy spectrum of the lead fluoride detector.

The association of a certain energy spectrum to a given set of events will be called *detector response*.

Before engaging directly in the discussion about the simulation of the A4

experiment, GEANT4, an instrument used for simulating, has to be presented shortly. GEANT4 is an object oriented programming toolkit for simulating the passage of particles through matter. Once the geometry and the processes to be simulated are defined, the toolkit makes use of Monte Carlo methods for tracking particles, either primaries or secondaries [18, 19]. How geometry and processes are defined is specified in Section 4.1. The meaning of tracking will be briefly summarised here.

Given a particle with its position and momentum in a certain medium and given a set of processes with their cross sections, it is possible to generate a *step*. A step is defined by: initial and final instant, initial and final position, initial and final momentum, deposited energy along the step, generated secondaries with respective momenta. The generation of a step is referred to as *stepping* and one *process* is an object class contributing to the stepping. Tracking one particle means generating a sequence of steps drawing a trajectory from the initial position until the particle is either absorbed by the material, or it decays, or it exits the defined geometry. The Monte Carlo methods and the cross section formulae used by GEANT4 processes for stepping are reported in detail in reference [19]. Among the variety of processes provided by GEANT4, only processes related to the electromagnetic interaction are used within this work.

At this point it is possible to enter into the discussion of the detector response simulation. The simulation is based both on GEANT4 and on an original approach developed independently within the work presented here.

The simulation of the A4 detector response can be divided in two main issues. One of these is the formation of electromagnetic showers with the consequent deposition of energy in the PbF_2 crystals. At the energy scale of the experiment and considering electrons as primary event particles, these showers contain electrons, positrons and photons with energy $\gtrsim 1$ keV (γ 's). The other issue is the radiation of Cherenkov light and its detection by the photomultipliers. In this case *optical photons*, with energies in the eV region, are involved. These have wavelengths of the order of visible light and are considered in GEANT4 as different particles than the γ 's.

For simplicity the energy deposition in the crystals resulting from the electromagnetic shower of one primary event particle will be called *calorimeter response* to that event. Similarly all aspects related to Cherenkov photons, namely their creation by particles in an electromagnetic shower, their propagation and their detection will be considered as a whole effect relating the deposition of energy to the detection of light. This effect will be referred to as *photomultiplier response*. The combination of the two phenomena, calorimeter and photomultiplier response, gives the detector response.

Generating the tracks for a whole electromagnetic shower using GEANT4 is relative fast in terms of CPU-time. Therefore simulating the value of deposited

energy in each crystal for every electron entering the calorimeter, i.e. simulating the calorimeter response, by tracking all particles in the electromagnetic cascade with GEANT4, is possible and offers a solution for the first issue cited above.

Yet simulating the Cherenkov shower using GEANT4 is very CPU-time consuming, because of the huge number of optical photons that have to be tracked. For this reason, including the full simulation of the Cherenkov effect in GEANT4 in order to have the detector response, that is calorimeter response and photomultiplier response together, does not allow to obtain a reasonable statistics in the simulated spectrum.

For taking into account also the effect of Cherenkov light radiation and detection a new approach was developed, combining the use of GEANT4 for simulating the calorimeter response with a parameterization of the photomultiplier response. The idea is that, given the value of deposited energy E_{dep} in a certain crystal, it is possible to determine, in a parametrized way, a probability distribution for the number of optical photons N_{ph} detected in the corresponding photomultiplier. Knowing this distribution N_{ph} can be sampled from it giving the photomultiplier response. For showing that this strategy is indeed possible and for obtaining such a parameterization, a restricted, though statistically significant, number of events was simulated with GEANT4 including the full simulation of the Cherenkov process. The results of this simulation were treated statistically showing that the parameterization is possible and the parametrized form for the distribution of N_{ph} given a value of the deposited energy E_{dep} has been determined.

In conclusion, for having the whole detector response, the simulation of the calorimeter response with GEANT4 is applied, giving for every event the energy deposited in each crystal. With these values of the deposited energy, the number of optical photons detected in each photomultiplier is sampled from the distribution determined according to the parameterization obtained previously.

In Section 4.1 the simulation of the energy deposition in the lead fluoride crystals using GEANT4 is described. The additional specification to this GEANT4 simulation for including the production, propagation and detection of Cherenkov optical photons are reported in Section 4.2. The derivation of the parameterization of the photomultiplier response is given in Section 4.3. Section 4.4 explains how to digitize and histogram the results of the detector response simulation, in order to make them comparable with the experimental energy spectrum.

4.1 Simulation of the deposition of energy in the PbF_2 crystals using GEANT4

For implementing a GEANT4 simulation one has to handle two main aspects. A geometry has to be defined, like explained in Section 4.1.1. The particles entering into the simulation and the processes to be simulated have to be declared, like reported in Section 4.1.2.

4.1.1 Geometry definition

Defining the geometry of the simulation means declaring which are the volumes the particles have to be tracked through. A volume is characterised by shape, dimensions, material, position and orientation with respect to the other defined volumes. The geometry of the simulation has been defined in order to reproduce as much as possible the experimental conditions. More specifically, the declared volumes represent ideally the set of material objects lying on the path one particle has to travel through getting from target into the detector.

In the following a list of the declared volumes will be given. The list order will respect the succession of material layers encountered by a particle travelling from the scattering point inside the target toward the PbF_2 crystals. Figure 4.1 gives a graphical representation of the simulated geometry.

- **Inner target.** The liquid hydrogen ($\ell\text{-H}_2$) volume contained in the target.

Shape: hemisphere.
Dimensions: radius, 94.75 mm.
Material: $\ell\text{-H}_2$.

- **Target container.** The aluminium (Al) container containing the liquid hydrogen.

Shape: hemispherical layer.
Dimensions: inner radius, 94.75 mm; thickness 0.25 mm.
Material: Al.

- **Scattering chamber.** Central thinner segment of the scattering chamber (see Section 3.2).

Shape: tube.
Dimensions: inner radius, 420 mm; thickness, 5 mm; length, 800 mm.
Material: Al.

Table 4.1: Materials defined in the simulation. In the part concerning the constituent elements, Z is the atomic number, A is the molar mass and w is the fraction mass. X_0 is the radiation length calculated by the toolkit.

Material	Symbol	Density g/cm^3	Constituent Elements				X_0 mm
			Symbol	$A[g/mole]$	Z	$w[\%]$	
Liquid hydrogen	$\ell-H_2$	$7.080 \cdot 10^{-2}$	H	1.01	1	100.0	$8.923 \cdot 10^3$
Aluminium	Al	2.700	Al	26.98	13	100.0	88.930
Air	–	$1.290 \cdot 10^{-3}$	N	14.01	7	70.0	$0.285 \cdot 10^6$
			O	16.00	8	30.0	
Lead fluoride	PbF_2	7.770	Pb	207.21	82	84.5	9.369
			F	19.00	9	15.5	

- **Calorimeter region.** Ring shaped air volume surrounding the scattering chamber and containing the detector.

Shape: tube.

Dimensions: inner radius, 425 mm; outer radius, 717 mm (that is 20 mm larger than R_0 , like defined in Appendix B); length, 800 mm.

Material: air.

- **Crystal frames.** The inner part of the aluminium frames supporting the crystals (see Figures 3.7, 3.6 and Section 3.3).

Shape: tube.

Dimensions: inner radius, 567 mm (142 mm from the scattering chamber); thickness, 10 mm; length, 700 mm.

Material: Al.

- **Crystals.** The lead fluoride crystals.

Shape: trapezoidal prism.

Dimensions: see Appendix B.

Material: PbF_2 .

The materials of the volumes are defined in the simulation giving density, temperature, pressure, constituting elements with their respective mass fraction w [20]. The toolkit uses this information to calculate the parameters which are needed for simulating the passage of particles through the materials, e.g. the radiation length X_0 . A summing of the defined materials with their parameters is given in Table 4.1.

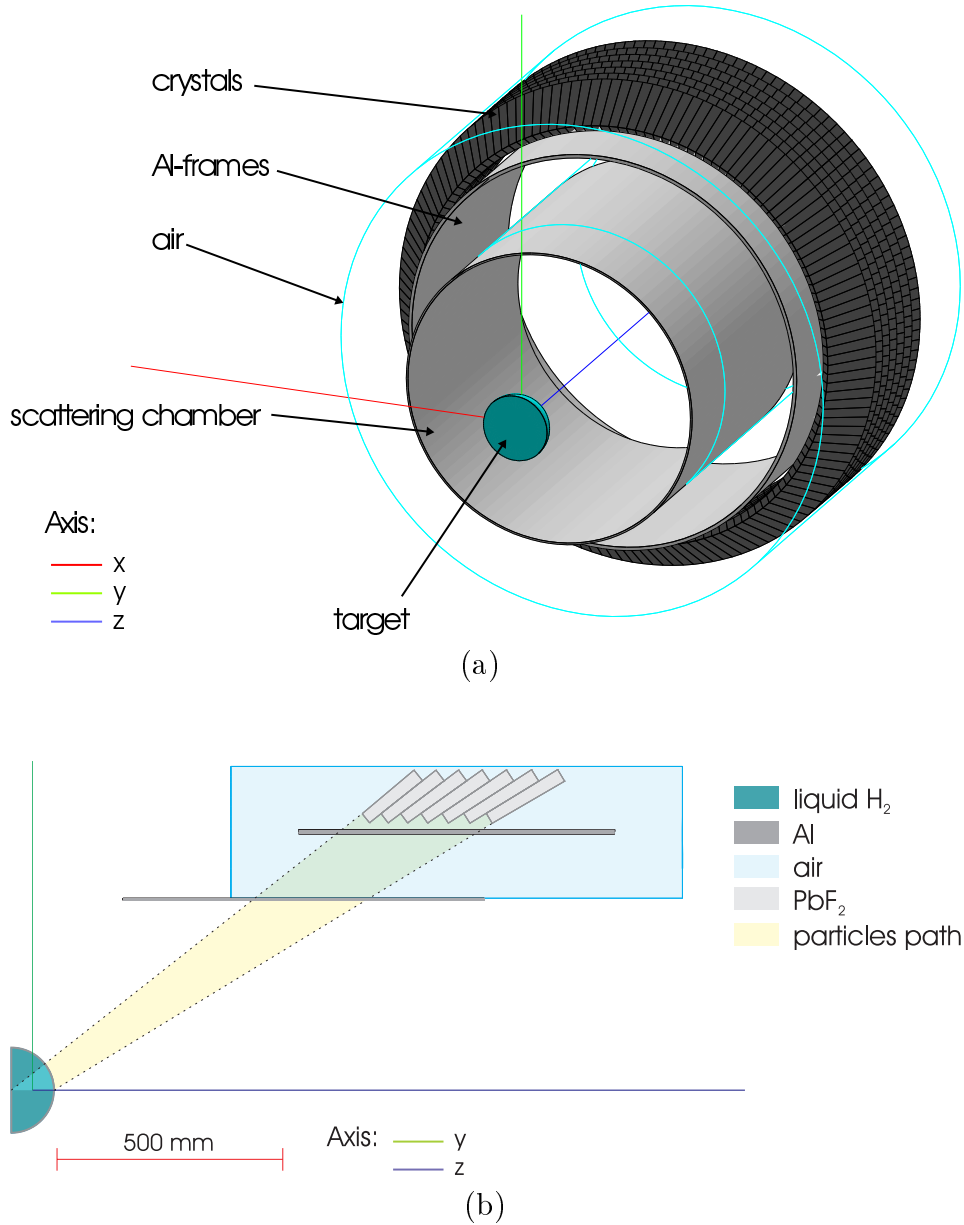


Figure 4.1: Geometrical setup of the simulation, GEANT4 graphical output view. The z-axis lies on the beam line with positive direction parallel to the momentum of electrons. The origin of the axes is the middle of the target.

(a) - Tridimensional view.

(b) - Slice view having cut with the yz-plane. Only the upper part is shown. The complete slice picture would be symmetric about the z-axis.

4.1.2 Particles and physical processes

In order to simulate the passage of particles through matter (that is tracking particles), one has to declare which particles have to be tracked and which processes have to be taken into account at tracking. The operations needed for stepping are then executed automatically by the toolkit.

The simulation of electromagnetic showers for determining the energy deposition in the crystals involves the following types of particle with relative processes. For each process, a short description of the stepping implementation features in GEANT4 is given. This part is based on reference [19], where many more details can be found.

γ : photon with energy $\gtrsim 1$ keV.

- Compton scattering: scattering of a photon off an atomic electron. For the total cross section an empirical formula is used, which reproduces the cross section data. The final state is sampled from the Klein-Nishina differential cross section per atom.
- Pair production: conversion of a γ into an (e^+, e^-) pair. Here also the total cross section per atom is parameterized in order to describe data. The final state is obtained according to a corrected Bethe-Heitler formula, for taking into account various effects (screening, Coulomb correction, presence of electron field).
- Photoelectric effect: ejection of an electron from a material after a photon has been absorbed by that material. It is simulated by using a parameterized photon absorption cross section to determine the mean free path, atomic shell data to determine the energy of the ejected electron, and the K-shell angular distribution to sample the direction of the electron. The relaxation of the atom is not simulated, but instead is counted as a local energy deposit.

e^-, e^+ : electron and positron.

- Multiple scattering: the multiple scattering of charged particles in matter. A condensed simulation algorithm is used, in which the global effects of the collisions are simulated at the end of a track segment. The global effects are the net displacement, energy loss and change of direction of the charged particle.

- Ionisation: provides the continuous and discrete energy losses of electrons and positrons due to ionization in a material. Above a given energy threshold for the ejected electron, the energy loss is simulated by the explicit production of delta rays by Møller scattering (e^-e^-), or Bhabha scattering (e^+e^-). Below the threshold the soft electrons ejected are simulated as continuous energy loss by the incident e^\pm , i.e. no secondaries are created.
- Bremsstrahlung: provides the energy loss of electrons and positrons due to the radiation of photons in the field of a nucleus. Like in the ionisation case, above a given photon energy threshold the explicit production of γ 's is simulated. Below the threshold the emission of soft photons is treated as a continuous energy loss.

e^+ : only for positron.

- Annihilation: simulates the in-flight annihilation of a positron with an atomic electron according to the cross section formula of Heitler. The atomic electron is supposed to be free and at rest. Contributions coming from three, or more, photons production are neglected.

4.2 Production and detection of Cherenkov light

For including the full simulation of the Cherenkov effect in the GEANT4 simulation, one has to take into account the production and propagation of the Cherenkov light. This is achieved declaring further geometry features and processes (Section 4.2.1). For taking into account the detection of the Cherenkov photons by the photomultipliers, the characteristics of the photomultipliers used in the experiment (their quantum efficiency) have to be embedded into the simulation, like specified in Section 4.2.2.

4.2.1 Producing and tracking optical photons

The Cherenkov effect occurring in the crystals can be simulated within GEANT4. The corresponding process class can be applied to all charged particles (in this

case electrons and positrons). It generates optical photons as secondaries. For tracking these, one needs to declare further geometrical features and processes.

Two optical properties have to be declared for the materials through which optical photons are tracked. They are refractive index and absorption length.

Secondly, unlike for the other particles, stepping optical photons becomes crucial at the border surface between two media with different optical properties. Therefore the tracking category of the simulation needs to know where such *optical surfaces* are and what kind of properties they have.

Finally the Cherenkov process and the processes able to track the optical photons have to be defined.

Material optical properties. The interesting volumes of the geometry for tracking the optical photons are the calorimeter region and the crystals inside of it (see Section 4.1.1 for definition of volumes). The materials constituting these two volumes are air and lead fluoride respectively.

Regarding the air, the absorption length was not defined. This means that optical photons are just not absorbed in this material. The refractive index was set to 1 independently from the wavelength.

Concerning lead fluoride, the absorption length was estimated for different wavelengths after three different radiation exposures, like reported in [15]. The irradiation values were 0, 100 and 200 Gy respectively. In the simulation the measurements after 100 Gy were used. They are shown in Figure 4.2. This value of irradiation corresponds to about 1000 hours of beam time without applying optical bleaching to the crystals, while in the experiment this is done more frequently. Nevertheless these data has been used in this work, in order to consider possible permanent shading of the crystals. However, the absorption length of PbF_2 , for radiation exposures between 0 Gy and 100 Gy varies only by some few percent [15].

Optical Surfaces. Similarly to the definition of a volume, it is possible to define an optical surface. The position and shape are determined by giving the volumes located at both sides of the surface. The properties one has to define concern the nature of material contact at the surface, the finish of the surface itself and the model to be used at tracking optical photons through it. Defining the nature of the contact means declaring whether the two materials involved are both dielectrics or one dielectric and one metal. The finish can be either polished or ground [20].

The optical surface relevant to the scope of this work is the crystals' surface. The materials at both sides are PbF_2 and air, hence the nature of the contact is dielectric-dielectric. The finish is defined as "ground painted". This means that a reflectivity index can be assigned to the surface, in order to simulate the effect of the reflective foils wrapped around the crystals (see Section 3.3.1). For tracking optical photons the so called UNIFIED model [21] was chosen. It

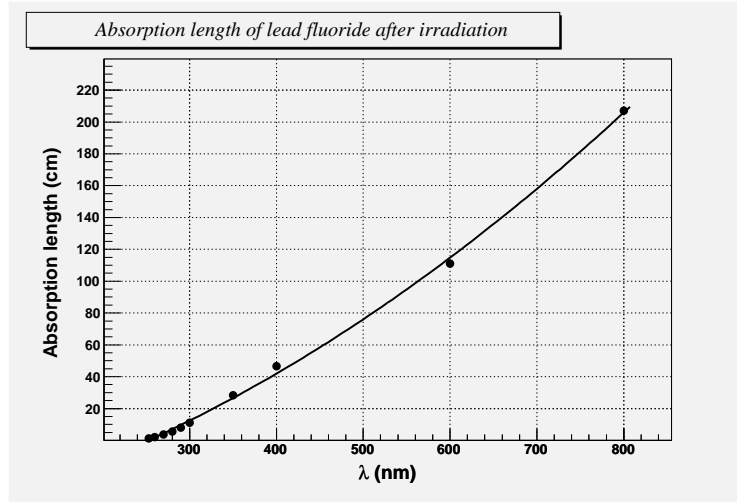


Figure 4.2: Absorption length of PbF_2 depending on the light wavelength. The data points are taken from [15] and correspond to a measurement after an irradiation of 100 Gy. The curve is a polynomial fit of the second order, which was used in the simulation to interpolate among the points.

provides the Monte Carlo algorithms for simulating the interaction of optical photons with dielectric surfaces.

Physical processes. Like in Section 4.1.2, the list of process classes used to produce and track optical photons is given in the following. More details can be found in references [19, 20].

- Cherenkov effect: produces optical photons as secondaries when a charged particle moves through a dispersive medium faster than the group velocity of light in that medium. The flux, spectrum, polarization and emission direction follow the well known formulae of the classical electrodynamics.
- Absorption: the process merely kills the particle. The empirical data for the absorption length are used (Figure 4.2). The absorption length is considered as the average distance traveled by a photon before being absorbed by the medium, i.e. it is the mean free path.

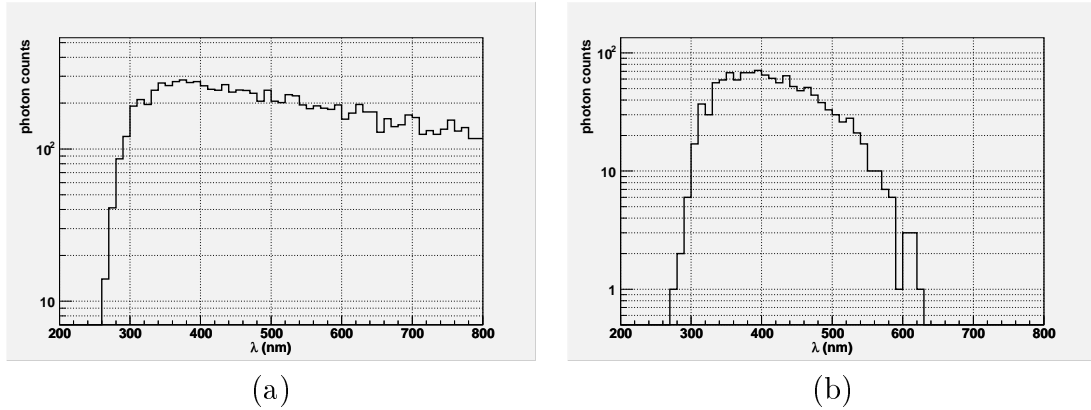


Figure 4.3: Simulated spectral response of the photomultipliers. The simulation was run shooting one electron with an energy of 734 MeV, i.e. the energy of elastically scattered electrons, onto the centre of one crystal of the fourth ring (central ring). Cherenkov photons are created and tracked.

(a) - Photon spectrum hitting the photomultiplier window.

The behaviour at short wavelengths is determined by the transmittance of lead fluoride. At longer wavelengths the spectrum follows the distribution of the Cherenkov light.

(b) - Photon spectrum detected by the photomultiplier. The shape reproduces the spectral sensitivity of the photomultipliers shown in the plot of Figure 3.9, as expected.

The ratio between the two heights of the maxima at 380 nm gives a value of 24% for the quantum efficiency at that wavelength.

- **Boundary Process:** steps optical photons through an optical surface according to a chosen model. In this work the UNIFIED model was used. The implementation is described in detail in reference [21].

4.2.2 Detecting optical photons

The simulation of the Cherenkov light detection by the photomultipliers is obtained in a straightforward manner. For each crystal, a new volume representing the photomultiplier tube is introduced into the geometry definition. The shape is a full cylinder with a radius of 14 mm (see Section 3.3.2). The axis of the tube coincides with the axis of the crystal prism. The contact surface between crystal and tube lies on the trapezoidal face of the crystal being at the external side of the calorimeter. The length of the tube is irrelevant as

well as its material.

The optical photons which are tracked into the tube are considered detected with a probability given by the quantum efficiency calculated according to equation 3.5.

Figure 4.3 shows an example of the simulated photon spectrum hitting the photomultiplier window - (a), and being detected - (b).

4.3 Deposited energy vs number of photoelectrons

As already specified at the beginning of this chapter, the photomultiplier response, that is the effect of the emission, propagation and detection of Cherenkov photons, must be treated separately from the GEANT4 simulation of the calorimeter response, i.e. deposition of energy in the crystals, because of the long duration of the tracking of optical photons within GEANT4. The simulations of the photomultiplier response should be treated in a parametrized way. This means that, given the calorimeter response of one event by the GEANT4 simulation, one should be able to estimate the photomultiplier response, hence the detector response, without further simulation (that is without further GEANT4 tracking).

In the work presented here, it has been shown that the parametrized treatment of the photomultiplier response is possible and a practical recipe for this treatment has been found. Two basic ideas have been used after being motivated, employing the GEANT4 simulation of the full Cherenkov effect. Be N_{ph} the number of photoelectrons emitted by the photocathode of the multiplier applied to one specific crystal. N_{ph} is a random variable with a certain probability distribution. The first idea is that this distribution depends only on the value E_{dep} of the deposited energy in that crystal. The second idea is that the shape of such distribution is gaussian. It has therefore a mean value \bar{N}_{ph} and a standard deviation σ_{ph} .

According to the first idea it is possible to determine two functions $\bar{N}_{ph}(E_{dep})$ and $\sigma_{ph}(E_{dep})$. Given a value of E_{dep} , these functions should allow one calculating the values for \bar{N}_{ph} and σ_{ph} respectively. After this, the distribution of the random variable N_{ph} is fixed and the photomultiplier response can be obtained just by sampling from such distribution.

In this paragraph, the two ideas proposed above are motivated and a form for the functions $\bar{N}_{ph}(E_{dep})$ and $\sigma_{ph}(E_{dep})$ is given.

About 1300 events were simulated with GEANT4 including the CPU-time consuming full tracking of the Cherenkov photons. The primary electrons were shot from random positions in the target, uniformly distributed along the beam line. The initial energy of the electrons was uniformly distributed

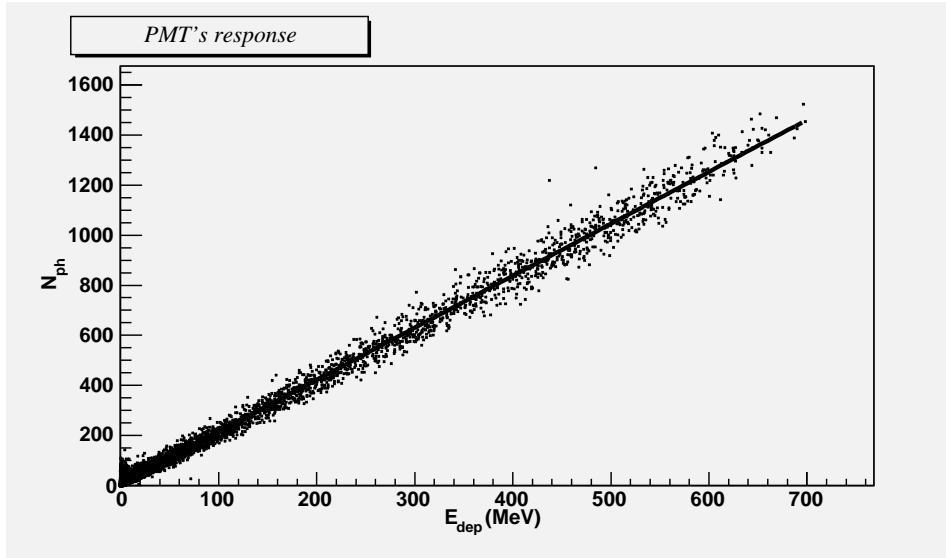


Figure 4.4: Number of photoelectrons in one phototube as a function of the deposited energy in the correspondent crystal. In the box the linear correlation coefficient r , the linear fit function and the numerical values of the fit parameters are given.

$$\begin{aligned}
 r &= 0.997. \\
 N_{ph} &= p_0 + p_1 \cdot E_{dep}, \\
 p_0 &= 6.59 \pm 0.13, \\
 p_1 &= (2.078 \pm 0.001)\text{MeV}^{-1}.
 \end{aligned}$$

between 150 and 850 MeV. The initial direction was chosen in such a way to hit uniformly the surface of one crystal of the fourth ring (see Section 4.1.1). For each event the values of E_{dep} and of the corresponding N_{ph} were saved in couples (E_{dep}, N_{ph}) for every crystal. The set of points of the (E_{dep}, N_{ph}) -plane obtained is represented in Figure 4.4.

In every event the largest part of the energy is deposited in one *central* crystal. That is typically the crystal through which the primary electron enters the calorimeter. The rest of the energy is deposited in the neighbouring crystals according to some development of the shower profile, which suffers stochastic fluctuations. In general the total deposited energy is less than the incoming electron energy since part of the shower could develop outside the crystals. Only the (E_{dep}, N_{ph}) -point due to the central crystal of one event can populate the large- E_{dep} region of Figure 4.4. The low- E_{dep} region in the same graph contains points due either to the central crystal of events with low primary electron energy or to the neighbouring crystals of whatsoever event. In other words, every event contributes with several points to the low- E_{dep} region while at most with one point to the large- E_{dep} region.

The value of E_{dep} in each particular crystal, central or neighbouring, depends on many factors. First of all, the initial energy of the primary electron contributes in determining the average shower profile and its fluctuations.

Furthermore the position of the entrance point of the electron on the crystal surface influences the portion of the shower that develops in each crystal and consequently the corresponding value of E_{dep} . For instance, the fraction of the total energy deposited in the central crystal for electron energies of about $700 \div 800$ MeV can vary between about $40 \div 50\%$, if the crystal is hit very close to its border, up to 80% or more in the case the electron enters in a well centered position. For lower electron energies these fractions are usually larger, because the transversal profile of the shower becomes narrower.

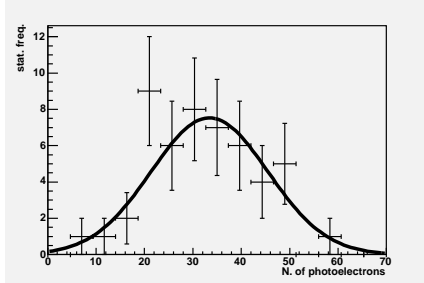
In addition the momentum direction of the incoming electron gives the average development direction of the cascade. The same initial energy and entrance position but different direction of development result in general in different E_{dep} values. In the GEANT4 simulation this direction is changed in two ways. Giving a random initial position in the target and being fixed the entrance position into the crystal, the angle between momentum direction and normal direction to the crystal surface acquires different values. Simulating the passage of the electron through the material from target to calorimeter deviates randomly the electron from the initial direction of motion.

The most important effect, though, is given by the shower fluctuations. Events having identical values for the previous parameters, i.e. initial electron momentum and entrance point, can end up in very different values of E_{dep} . This happens just because the development of an electromagnetic cascade is a stochastic process.

As a consequence, the same value of E_{dep} in one crystal can be caused in many different ways. According to the first one of the two basic ideas given above, the way the energy E_{dep} has been deposited in a crystal does not affect the distribution of the number of detected Cherenkov photons N_{ph} by the corresponding photomultiplier, since this distribution depend only on the value of E_{dep} . In other words, given a certain value of E_{dep} , N_{ph} has always the same distribution, independently from how that particular value of E_{dep} was achieved. Figure 4.4 is a justification of such assumption because the points on the graph show a strong correlation between E_{dep} and N_{ph} . Quantitatively, the linear correlation coefficient r is 0.997. This means that the mean value \bar{N}_{ph} can be considered as a linear function of E_{dep} . Hence the form for $\bar{N}_{ph}(E_{dep})$ is just the linear fit given in Figure 4.4.

Justifying rigorously the second assumption is more difficult. To test how N_{ph} is distributed for a given value of E_{dep} , one should plot the statistical frequency of the single values of N_{ph} for many events, all having the same value of E_{dep} . Since the electromagnetic cascade must be also simulated together with the photomultiplier response, one obtains unavoidably different random

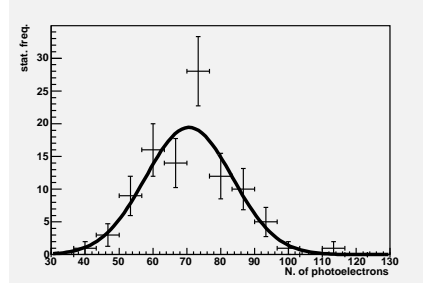
$$E_{dep} = (10 \pm 0.1)\text{MeV:}$$



$$\chi^2/n_d = 4.0/8 \quad \bar{N}_{ph}^{\text{fit}} = 33.4$$

$$p = 86\% \quad \sigma_{ph}^{\text{fit}} = 12.1$$

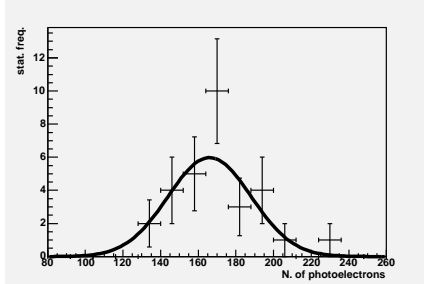
$$E_{dep} = (30 \pm 1)\text{MeV:}$$



$$\chi^2/n_d = 6.9/8 \quad \bar{N}_{ph}^{\text{fit}} = 70.7$$

$$p = 55\% \quad \sigma_{ph}^{\text{fit}} = 12.8$$

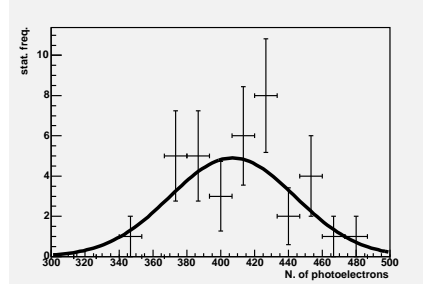
$$E_{dep} = (80 \pm 1)\text{MeV:}$$



$$\chi^2/n_d = 3.9/5 \quad \bar{N}_{ph}^{\text{fit}} = 166$$

$$p = 56\% \quad \sigma_{ph}^{\text{fit}} = 22.1$$

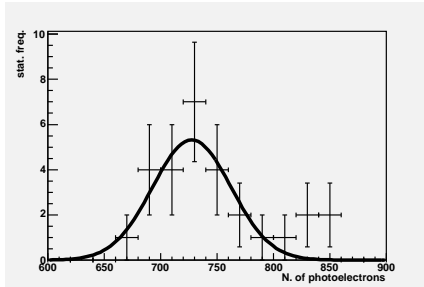
$$E_{dep} = (200 \pm 5)\text{MeV:}$$



$$\chi^2/n_d = 5.7/7 \quad \bar{N}_{ph}^{\text{fit}} = 407$$

$$p = 57\% \quad \sigma_{ph}^{\text{fit}} = 37.1$$

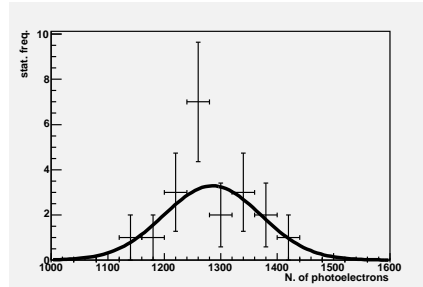
$$E_{dep} = (350 \pm 7)\text{MeV:}$$



$$\chi^2/n_d = 5.4/7 \quad \bar{N}_{ph}^{\text{fit}} = 728$$

$$p = 61\% \quad \sigma_{ph}^{\text{fit}} = 34.8$$

$$E_{dep} = (600 \pm 10)\text{MeV:}$$



$$\chi^2/n_d = 3.4/5 \quad \bar{N}_{ph}^{\text{fit}} = 1285$$

$$p = 64\% \quad \sigma_{ph}^{\text{fit}} = 85.8$$

Figure 4.5: Statistical frequencies of the number of photoelectrons for different values of the deposited energy E_{dep} . On top of each histogram the corresponding $(E_{dep} \pm \delta E_{dep})$ -interval is given. The vertical error bars are given by the squared root of the bin content. On the bottom the parameters $\bar{N}_{ph}^{\text{fit}}$ and σ_{ph}^{fit} of the gaussian fit are reported. The value χ^2/n_d is the χ^2 of the fit divided by the number of degrees of freedom n_d (number of data points minus number of fit parameters). The other parameter is the p -value of the goodness-of-fit test [22].

values of E_{dep} for each event. For having a statistical sample of N_{ph} , then, one needs to take the points of Figure 4.4, that are included in some interval $E_{dep} \pm \delta E_{dep}$, instead of just those which correspond to some exact value E_{dep} . In order to have a larger sample one should consider a wider interval of E_{dep} , so that more points are included. On the other hand, the sample distribution one obtains with a large δE_{dep} derives from the superposition of the distributions corresponding to different values of E_{dep} , which have different values for \bar{N}_{ph} and σ_{ph} . Therefore the smaller δE_{dep} is, the better the obtained sample distribution would represent the distribution of N_{ph} corresponding to one single value of E_{dep} .

Mediating between these two issues, it is possible to get a result like in Figure 4.5. The sample distributions for the given intervals of E_{dep} are shown. The value of δE_{dep} increases with increasing central value E_{dep} . Such a choice was imposed by the poorer statistics in the large- E_{dep} region of the (E_{dep}, N_{ph}) -plot (Figure 4.4). This does not constitute a very cumbersome problem because the sample variances also become larger with larger E_{dep} . If the variation of the mean value and of the standard deviation of N_{ph} within the E_{dep} -interval are small with respect to the absolute value of the standard deviation at E_{dep} , then the superposition of the different distributions in $E_{dep} \pm \delta E_{dep}$ remains a good approximation of the single- E_{dep} distribution.

Estimating the error on the statistical frequency with its squared root, a gaussian curve was fitted on each histogram of Figure 4.5 and the p -value of the goodness-of-fit test [22] was calculated. The statistical samples are not very large but all p -values are greater than 55% and, except for one case, smaller than 64%, which is in agreement with the assumption of the gaussian form for the distribution of N_{ph} .

In order to find a form for the function $\sigma_{ph}(E_{dep})$, sample values of N_{ph} for different values of E_{dep} are needed. For each value of E_{dep} , the sample values of N_{ph} are given by the (E_{dep}, N_{ph}) -points of Figure 4.4 having E_{dep} contained in some interval $E_{dep} \pm \delta E_{dep}$.

Out of this sample the estimator $s^2(E_{dep})$ for $\sigma_{ph}^2(E_{dep})$ was calculated according to

$$s^2(E_{dep}) = \frac{1}{n} \sum_{i=1}^n (N_{ph,i} - \bar{N}_{ph}(E_{dep}))^2, \quad (4.1)$$

where $N_{ph,i}$ ($i=1, \dots, n$) are the sample values of N_{ph} and $\bar{N}_{ph}(E_{dep})$ is calculated according to the fit given in Figure 4.4. For this reason, $s^2(E_{dep})$ is not the sample variance and will be considered as an unbiased estimator of $\sigma_{ph}^2(E_{dep})$ without multiplying it by the usual factor $n/(n-1)$. This is because $\bar{N}_{ph}(E_{dep})$ is not the mean of the sample values $N_{ph,i}$ ($i=1, \dots, n$) but the estimation of \bar{N}_{ph} obtained by using a large statistical sample. Hence, within the small sample $\{N_{ph,i}\}$, $\bar{N}_{ph}(E_{dep})$ can be considered as the ‘‘real value’’ of \bar{N}_{ph} .

The variance $\text{var}(s^2)$ of s^2 is given by

$$\text{var}(s^2(E_{dep})) = \frac{1}{n}(\mu_4 - \mu_2^2), \quad (4.2)$$

where μ_k is the k -th central momentum of the N_{ph} distribution. Since the variable N_{ph} is supposed to be Gauss distributed it holds:

$$\begin{aligned} \mu_2 &= \sigma_{ph}^2, \\ \mu_4 &= 3\sigma_{ph}^4. \end{aligned} \quad (4.3)$$

Substituting (4.3) in (4.2) and considering the standard deviation of s^2 as its statistical error $(\delta s^2)_{\text{stat}}$, this assumes the form:

$$(\delta s^2)_{\text{stat}} = \sqrt{\frac{2}{n}} s^2, \quad (4.4)$$

remembering that s^2 is the estimator for σ_{ph}^2 .

The quantity $\bar{N}_{ph}(E_{dep})$ is also known with a statistical error $\delta \bar{N}_{ph}(E_{dep})$, inferred by the error on the fit parameters given in Figure 4.4. Such an error on $\bar{N}_{ph}(E_{dep})$ propagates also onto $s^2(E_{dep})$, which is therefore affected by a further error $(\delta s^2)_{\bar{N}}$. Expanding the expression (4.1), taking the first derivative with respect to \bar{N}_{ph} and multiplying by $\delta \bar{N}_{ph}$ gives the estimation of $(\delta s^2)_{\bar{N}}$,

$$(\delta s^2)_{\bar{N}} = 2 |\bar{N}_{ph} - \langle N_{ph,i} \rangle| \cdot \delta \bar{N}_{ph}, \quad (4.5)$$

where $\langle N_{ph,i} \rangle$ is the sample mean of $\{N_{ph,i}\}$. Altogether the estimation for the error of s^2 is given considering (4.4) and (4.5):

$$(\delta s^2)_{\text{tot}} = \sqrt{(\delta s^2)_{\text{stat}}^2 + (\delta s^2)_{\bar{N}}^2}. \quad (4.6)$$

Sample values of $s^2(E_{dep})$ have been obtained from samples of \bar{N}_{ph} corresponding to E_{dep} intervals $E_{dep} \pm \delta E_{dep}$, as follows. The E_{dep} range between 0 and 700 MeV has been subdivided into 25 subranges of the same width. The central E_{dep} value of each subrange has been taken together with a width δE_{dep} growing linearly with E_{dep} from 1 MeV to 5 MeV as E_{dep} ranges from 0 to 700 MeV. Among these 25 intervals $E_{dep} \pm \delta E_{dep}$, only those containing more than 5 values of \bar{N}_{ph} were used to calculate $s^2(E_{dep})$. These sample values of $s^2(E_{dep})$ with their errors are plotted in Figure 4.6. In all of these samples $(\delta s^2)_{\bar{N}}$ is less than about 6% of $(\delta s^2)_{\text{stat}}$, which is a confirmation of what has been stated above with respect to the estimation of σ_{ph}^2 by the estimator $s^2(E_{dep})$. A linear function has been fitted to the data and the value of the fit parameters are given on the bottom of the graph in Figure 4.6. The reduced χ^2 and the goodness-of-fit were also estimated. The p -value amounts to 44%,

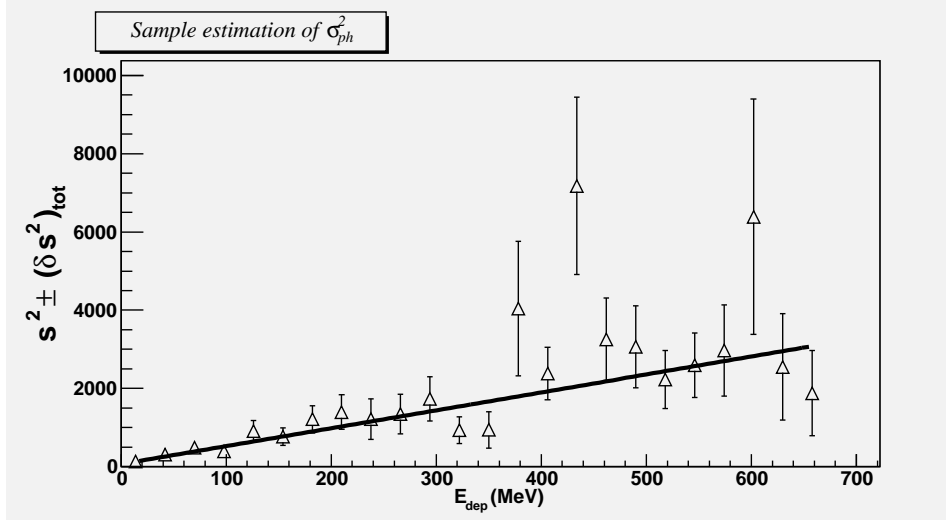


Figure 4.6: Sample estimation of σ_{ph}^2 as a function of the deposited Energy. In the box the values of the linear fit parameters are given together with the χ^2 divided by the number n_d of degrees of freedom and the p -value of the goodness-of-fit test [22].

$$\begin{aligned}
 s^2 &= a_0 + a_1 \cdot E_{dep} , \\
 a_0 &= 64.8 \pm 11.3 , \\
 a_1 &= (4.58 \pm 0.40) \text{MeV}^{-1} . \\
 \frac{\chi^2}{n_d} &= \frac{22.38}{22} , \\
 p &= 0.44 .
 \end{aligned}$$

thus the linear dependence of s^2 , i.e. σ_{ph}^2 , on E_{dep} is assumed to be a reasonable hypothesis. This is the needed dependence of σ_{ph} on the deposited energy E_{dep} , that is the function $\sigma_{ph}(E_{dep})$.

To summarize, in this section a parameterization for simulating the photo-multiplier response has been presented. That is, given the value of deposited energy E_{dep} in one crystal simulated with GEANT4, the effect of the emission, propagation and detection of Cherenkov photons onto the overall detector response is simulated without using the full GEANT4 simulation including Cherenkov effect but sampling the number of detected photoelectrons N_{ph} from a gaussian distribution. The mean value \bar{N}_{ph} and the variance σ_{ph}^2 of this gaussian distribution are linear functions of the deposited energy E_{dep} . Within this work, this approach has been motivated statistically using the results of a GEANT4 simulation including the Cherenkov process and the parameters of the linear functions $\bar{N}_{ph}(E_{dep})$ and $\sigma_{ph}^2(E_{dep})$ have been determined.

4.4 Digitization and histogramming

After simulating an event, one has the value of N_{ph} for each crystal as an output. That is the number of photoelectrons emitted by the photocathode of the corresponding photomultiplier. As discussed in Section 3.4, N_{ph} is proportional to the time integral of the current signal of the photomultiplier over a time window τ . In the real experiment, this value is summed over a 3×3 matrix of crystals and digitized. In order to obtain a histogram which is comparable with the experimental spectrum, a similar procedure must be applied to the simulated values of N_{ph} .

First, every experimental spectrum corresponds to one single channel, i.e. crystal with corresponding photomultiplier tube. For reproducing a spectrum, a channel must be chosen and all events that contribute to that channel must be simulated. An event gives a contribution to a channel if N_{ph} has a local maximum in that channel like specified in Section 3.4. Therefore after simulating an event, if the selected channel happens to be a local maximum, the histogram representing the simulated spectrum is updated.

Second, the 9 values of N_{ph} corresponding to the 3×3 matrix of crystals centred on the selected channel are summed giving the total value $N_{ph}^{3 \times 3}$. This value is a real number, because the N_{ph} 's are sampled from a continuous gaussian distribution. This is an advantage, because binning problems due to digitization of discretized values are avoided.

The final step is filling one of the 256 bins in the histogram. To do that, $N_{ph}^{3 \times 3}$ must be rescaled into a value b corresponding to one ADC-channel of the experimental histogram. For rescaling, two reference points in $N_{ph}^{3 \times 3}$ -space must be matched to two reference points in b -space. The zero of $N_{ph}^{3 \times 3}$ corresponds to the physical zero b^{off} of the ADC (offset), which is a fixed parameter of the readout electronics. The other point is given by the position of the elastic peak. An ADC-channel b^{el} , corresponding to the central ADC value of the elastic scattering peak, is selected by calibrating the detector like explained in Section 3.4 (typically $b^{el} = 170$). The corresponding $N_{ph}^{3 \times 3}$ -value N_{ph}^{el} has been obtained by simulating 5000 elastic events and taking the mean value of the $N_{ph}^{3 \times 3}$'s. The relation between $N_{ph}^{3 \times 3}$ and b is then simply:

$$b = b^{off} + \frac{b^{el} - b^{off}}{N_{ph}^{el}} \cdot N_{ph}^{3 \times 3} . \quad (4.7)$$

One event contributes to the simulated histogram only if it gives a value of b ranging from 0 to 256. In the experimental histogram, one event contributes if its time integrated current signal is greater than a certain threshold, as explained in Section 3.4. The b value corresponding to the threshold is always greater than 0 (typically about $40 \div 50$). For having such a b value, the scattered electron energy must be of the order of ($200 \div 250$) MeV.

Chapter 5

Simulation of physical processes

From here on, any interaction of the beam electrons in the target, which produces an event, that is a primary electron with given kinematics, will be called *physical process*. The theoretical knowledge of the physical processes, i.e. of their cross sections, allows the simulation of such processes, which in this context means the random sampling of events from their cross sections. The algorithm in charge of executing such a sampling will be called *event generator* and the output of the algorithm *theoretical spectrum*. Since the theoretical spectrum is determined by the set of physical processes that are simulated, an event generator can be considered equivalent to the set of physical processes it simulates.

The ultimate scope of this work is the study of the contribution of physical processes to the experimental spectrum, particularly in the low energy region, in order to extract the parity violation asymmetry in the electroproduction cross section of the $\Delta(1232)$ resonance. The simulation of the detector response described in the previous chapter provides a tool for comparing the theoretical spectrum given by any event generator with the experimental spectrum.

One event generator has been implemented and its theoretical spectrum compared with the experimental spectrum. A good agreement is found for the energy range from the $\Delta(1232)$ resonance peak ($E'=440$ MeV) up to above the elastic scattering peak ($E'>800$ MeV). More work has to be done for having a better agreement between theoretical and experimental spectrum in the low energy range. In this chapter the features of this event generator are presented.

5.1 Kinematical region

Like stated in Section 4.4, all events contributing to the spectrum of one selected channel must be simulated. The kinematical ranges of the primary electrons have to be fixed accordingly.

Solid angle

An event gives a contribution to a channel Ch if the number of photons N_{ph}^{Ch} detected by the photomultiplier of Ch is a local maximum, like specified in Section 3.4. N_{ph}^{Ch} can be a local maximum if the primary electron enters the detector through the surface of the corresponding crystal or of the surrounding ones.

To select the region of entrance of the primary electron into the detector, the primary momentum direction must be generated with a polar angle θ and an azimuthal angle ϕ contained in an interval $(\theta_0 - \Delta\theta/2, \theta_0 + \Delta\theta/2)$ and $(\phi_0 - \Delta\phi/2, \phi_0 + \Delta\phi/2)$, respectively. Fixing these two intervals is equivalent to define a rectangle on the surface of the detector onto which the electrons are shot. The rectangle has to contain the entrance (directed toward the target) surface of the crystal corresponding to the selected channel Ch . More specifically the rectangle has to be wider than the surface of the crystal, i.e. some electrons are shot outside the surface of the crystal, in order to consider the contributions to the spectrum coming from electrons hitting the surface of neighbouring crystals. The criterion for deciding the dimensions of this rectangle is that primary electrons, hitting the surface of the calorimeter outside the rectangle can not contribute to the spectrum, or their contribution is quite negligible.

The values θ_0 and ϕ_0 were fixed according to the direction of the line going through the centre of the target and the centre of the selected crystal's surface. The chosen crystal belongs to the fourth ring, which is the central one. Therefore, according to table B.1, θ_0 was set to 34.8° . Since all events to be simulated are generated by ϕ -symmetric processes, ϕ_0 has to correspond to the centre of an arbitrary frame.

The widths $\Delta\theta$ and $\Delta\phi$ were chosen equal to 2.4° and 2.6° , respectively. To fix these values the following procedure was followed. Some thousands events were simulated shooting primary electrons from a uniformly distributed random position in the target and with an initial energy of 734.5 MeV, which is the largest initial energy (*elastic energy*) of the electrons contributing to the spectrum at the scattering angle θ_0 . By changing the momentum direction angles θ and ϕ , one decides onto which point of the crystal surface the electrons are shot. The angle θ (ϕ) was set equal to θ_0 (ϕ_0). The other angle ϕ (θ) was set equal to $\phi_0 + \Delta\phi/2$ or $\phi_0 - \Delta\phi/2$ ($\theta_0 + \Delta\theta/2$ or $\theta_0 - \Delta\theta/2$). $\Delta\phi$ ($\Delta\theta$) was chosen in order to shoot the electrons to the border of the crystal Ch and then increased to hit other positions outside the crystal, i.e. the surface of one neighbouring crystal. For each value of ϕ (θ), 1000 events were simulated and the number of events, where N_{ph}^{Ch} was local maximum, was counted. This was repeated until a value for $\Delta\phi$ ($\Delta\theta$) was found, such that there were no more events, within the 1000 simulated, with N_{ph}^{Ch} as local maximum. The final values obtained for $\Delta\theta$ and $\Delta\phi$ were those given above (2.4° and 2.6° , respectively).

Sampling the momentum direction of the primary electrons within these intervals for θ and ϕ , many electrons hit the detector outside the surface of the crystal Ch . In fact, only about 30% of the events having a primary momentum direction within this range contribute to the simulation. This means that the majority of the simulated events are lost, since they do not contribute to obtain a better statistics. However generating the events into such a wide solid angle ensures that all primary kinematical configurations, which possibly contribute to the spectrum, are included in the simulation.

All physical processes to be simulated are ϕ -symmetric, thus $\Delta\phi$ will appear in the cross section formulae just as a multiplicative factor. On the contrary, all cross sections depend on θ and have to be integrated over the θ interval. It is therefore convenient to define:

$$\begin{aligned}\theta_A &\equiv \theta_0 - \Delta\theta/2, \\ \theta_B &\equiv \theta_0 + \Delta\theta/2.\end{aligned}$$

Energy range

The upper limit for the energy of primary electrons is given by the simulated processes. For instance, for the elastic scattering off the proton, the electrons with the highest final state energy are those, that have lost no energy by radiation of real photons. Their energy is thus limited by the kinematics of the elastic scattering (Equation (A.7)).

More attention has to be paid for the lower energy limit of the primary electrons E'_{low} . This is the lowest final energy value which can be sampled by the event generator from the cross sections of the various simulated processes. In the experiment, the corresponding limit is given by the low energy acceptance of the detector. This is fixed in turn by an electronic threshold (see Section 3.4). As already said at the end of Section 4.4, according to the detector response simulation, this threshold corresponds to primary energies of about $(200 \div 250)$ MeV. For simulating all events contributing to the spectrum, E'_{low} must be smaller than such values. Depending on the process, the value for E'_{low} ranges between 100 MeV and 120 MeV.

5.2 Bremsstrahlung and straggling function

The simulation of the detector response to a scattered electron of the beam begins by tracking the electron just after its scattering off a proton at some point in the target. Although, the electron travels through the target until the scattering point. The effect of the passage through this layer of material is not taken into account in the detector response simulation.

The interaction with the liquid hydrogen in the target affects the momentum of the beam electrons. The deflection from the original beam direction is

not considered in this work. The energy straggling is due almost completely to bremsstrahlung, because at the beam energy of the experiment (854.3 MeV) the energy loss per ionisation is negligible with respect to the effect of external radiation [22].

If the beam energy before hitting the target is E_0 , after travelling a distance t through the target (where t is expressed in units of radiation length), the energy of the beam electrons will be distributed with a certain probability density function (p.d.f.) $I_e(E_0, E, t)$. The energy E is the same as defined in Appendix A, then it is the energy of the electron just before it scatters off a proton. The p.d.f. $I_e(E_0, E, t)$ is called straggling function and, considering only the energy loss due to bremsstrahlung, is given by Mo and Tsai [23]:

$$I_e(E_0, E, t) = \frac{bt}{E_0 - E} \left[\frac{E}{E_0} + \frac{3}{4} \left(\frac{E_0 - E}{E_0} \right)^2 \right] \left(\ln \frac{E_0}{E} \right)^{bt}, \quad (5.1)$$

with $b=4/3$. In other words, for one electron of initial energy E_0 that passes through a target layer of thickness t , the differential quantity $I_e(E_0, E, t) dE$ represents the probability that the energy of the electron be in the interval $(E, E+dE)$.

The function $I_e(E_0, E, t)$ is not analytical in $E = E_0$. To treat this singularity the E -interval of definition $(0, E_0)$ has been divided into two intervals $(0, E_0 - \Delta E_s)$ and $(E_0 - \Delta E_s, E_0)$, respectively. Within the first interval the function $I_e(E_0, E, t)$ can be integrated numerically and can be used for sampling E . The larger the value of ΔE_s is, the faster is the numerical integration and the more precise can be the sampling.

All electrons having an energy inside the interval $(E_0 - \Delta E_s, E_0)$ have been treated as if they had the beam energy E_0 . Using this approximation, the probability $J_e^{\Delta E_s}(E_0, t)$ for one electron of still having all the beam energy E_0 after travelling through a layer t of target material is:

$$J_e^{\Delta E_s}(E_0, t) = 1 - \int_0^{E_0 - \Delta E_s} dE I_e(E_0, E, t), \quad (5.2)$$

because of the normalization of $I_e(E_0, E, t)$. Such an approximation is valid only if two requirements are fulfilled.

1. The cross sections of the scattering processes to be simulated (e.g. elastic and inelastic e - p scattering) must not vary too much in the energy range $(E_0 - \Delta E_s, E_0)$.
2. For the same processes, the variation of E in the interval of width ΔE_s causes a variation in the final energy E' of the scattered electron according to Equations (A.7) and (A.8). The corresponding interval of E' will have a width $\Delta E'_s$ depending on E' or, equivalently, on E . $\Delta E'_s$ must be small in comparison with the energy resolution of the detector $\Delta E'$ at E' given by Equation 3.4.

Considering elastic scattering and inelastic scattering at the $\Delta(1232)$ -peak in the polar angle interval $\theta \in (30^\circ, 40^\circ)$ and choosing $\Delta E_s = 0.1$ MeV, the difference in the cross sections between $E = E_0 - \Delta E_s$ and $E = E_0$ is at most about 0.1%.

In the same polar angle interval and with W ranging from M_p up to 1450 MeV (see Appendix A for definitions), one has always $\Delta E'_s < 0.1$ MeV. The detector energy resolution in the corresponding E' interval, which is (167 MeV, 761 MeV) according to A.7 and A.8, satisfies $13 \text{ MeV} \leq \Delta E' \leq 28 \text{ MeV}$. In conclusion, with the chosen value of ΔE_s , the cut on the domain of $I_e(E_0, E, t)$ can have no visible influence on the simulated spectrum.

So far the effect of energy straggling in the target input window has been considered just for the elastic e - p scattering. However it is planned to upgrade the event generator in order to take care of the energy straggling also for the cases of inelastic scattering off proton and scattering off aluminium.

5.3 Elastic electron scattering off the proton

5.3.1 Unradiated cross section

The elastic interaction of massless spin 1/2 electrons with point-like spinless protons of finite mass is described by the Mott cross section [24, 25]. The form of the Mott cross section in the approximation of one virtual photon exchange is¹:

$$\left. \frac{d^2\sigma}{d\Omega} \right|_{Mott} (E, \theta) = \frac{\alpha^2}{4E^2 \sin^4 \frac{\theta}{2}} \cdot \frac{E'}{E} \cos^2 \frac{\theta}{2}, \quad (5.3)$$

where $\alpha = e^2/4\pi \simeq 1/137$ is the fine structure constant.

Considering that the proton is also a spin 1/2 particle and that it presents an extended structure, the Rosenbluth formula must be introduced. Thus the twofold differential cross section for the elastic electron scattering off protons is given by:

$$\left. \frac{d^2\sigma}{d\Omega} \right|_{Ros} (E, \theta) = \left. \frac{d^2\sigma}{d\Omega} \right|_{Mott} (E, \theta) \cdot \left[\frac{G_E^2(Q^2) + \tau G_M^2(Q^2)}{1 + \tau} + 2\tau G_M^2(Q^2) \tan^2 \frac{\theta}{2} \right]. \quad (5.4)$$

In this equation the kinematical factor τ is

$$\tau = \frac{Q^2}{4M_p^2}. \quad (5.5)$$

¹The Planck constant is considered as $\hbar = 1$.

The electromagnetic form factors, which are used in the work presented here, are calculated according to the dipole fit [24]:

$$G_E(Q^2) = \frac{G_M(Q^2)}{2.79} = G^{\text{dipole}}(Q^2), \quad (5.6)$$

$$G^{\text{dipole}}(Q^2) = \left(1 + \frac{Q^2}{0.71 \text{GeV}^2}\right)^{-2}. \quad (5.7)$$

5.3.2 Radiative corrections to elastic scattering

The QED radiative corrections to elastic scattering can describe two effects in the spectrum. On the one hand the peak corresponding to the elastic line is modified with respect to what would be expected from the cross section without radiative corrections (5.4). On the other hand the radiation of hard real photons can result in the loss of a large energy amount ω by the electron. Because of this, a radiative tail at energies lower than the elastic peak appears in the spectrum.

The radiative tail from the elastic peak can be calculated using the peaking approximation, as shown by Mo and Tsai [23]. Contributions coming from the radiation of photons by the incident electron and by the scattered electron can be treated independently (the interference between the two contributions is neglected), since the scattering angle is sufficiently large [26]. The Feynman diagrams corresponding to these two contributions are shown on bottom of Figure 5.1, on the left and on the right, respectively.

After choosing an energy cutoff ΔE_r for defining the peak of elastically scattered electrons, the differential cross section of the tail is integrated over ω from 0 to ΔE_r and the vertex correction and the vacuum polarization are added (vertex correction and vacuum polarization are shown diagrammatically in the second line of Figure 5.1). The result is the corrected elastic cross section:

$$\left. \frac{d^2\sigma}{d\Omega} \right|_{\text{peak}}(E, \theta) = (1 + \delta(\Delta E_r, E, \theta)) \left. \frac{d^2\sigma}{d\Omega} \right|_{\text{Ros}}(E, \theta). \quad (5.8)$$

The form for $\delta(\Delta E_r, E, \theta)$ is given by Tsai [27]. Assuming the peaking approximation and neglecting the radiation from the proton current one has:

$$\begin{aligned} \delta(\Delta E_r, E, \theta) = & -\frac{\alpha}{\pi} \left[\frac{28}{9} - \frac{13}{6} \ln \frac{Q^2}{m_e^2} + \left(\ln \frac{E}{\Delta E_r} + \ln \frac{E'}{\Delta E_r} \right) \left(\ln \frac{Q^2}{m_e^2} - 1 \right) \right. \\ & \left. + \frac{1}{2} \left(\ln \frac{E'}{E} \right)^2 \right], \end{aligned} \quad (5.9)$$

where m_e is the electron mass and E' is calculated by means of (A.7).

For $\omega > \Delta E_r$, the differential cross section describing the scattering of the electron accompanied by the emission of hard photons can be integrated in the

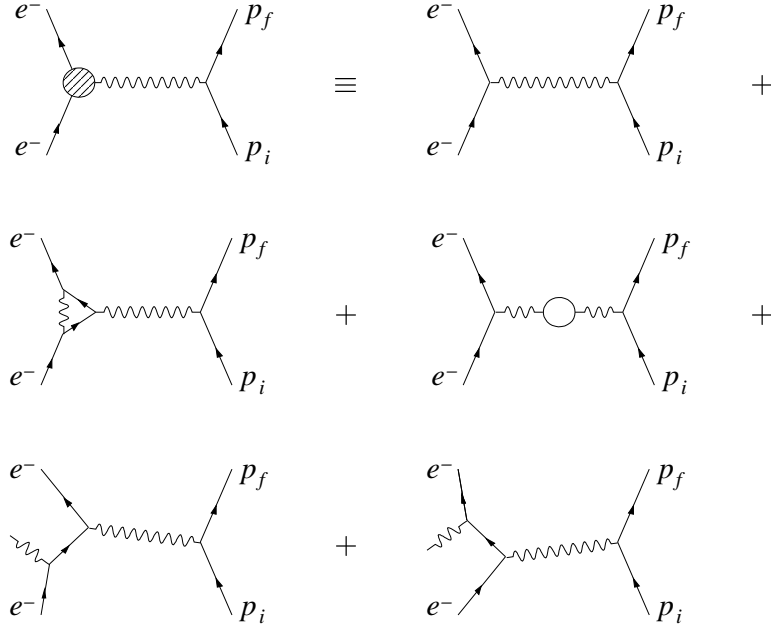


Figure 5.1: Feynman diagrams for calculating the radiative corrections on the elastic electron-proton scattering. Starting from the top on the right and following the reading order: elastic process, vertex correction, vacuum polarization, initial state radiation and final state radiation.

peaking approximation over the photon solid angle. This gives the inclusive threefold differential cross section for the radiative tail from the elastic peak. In the notation of [26], this cross section assumes the form:

$$\begin{aligned} \left. \frac{d^3\sigma}{d\Omega dE'} \right|_{tail}(E, E', \theta) &= \frac{t_s}{\omega_s} \frac{M_p + (E - \omega_s)(1 - \cos \theta)}{M_p - E'(1 - \cos \theta)} \left. \frac{d^2\sigma}{d\Omega} \right|_{Ros}(E - \omega_s, \theta) \\ &+ \frac{t_p}{\omega_p} \left. \frac{d^2\sigma}{d\Omega} \right|_{Ros}(E, \theta). \end{aligned} \quad (5.10)$$

Here ω_s and ω_p are the initial and final photon energies, respectively:

$$\begin{aligned} \omega_s &= \frac{-Q^2 + 2M_p(E - E')}{2[M_p - E'(1 - \cos \theta)]}, \\ \omega_p &= \frac{-Q^2 + 2M_p(E - E')}{2[M_p + E(1 - \cos \theta)]} \end{aligned}$$

and

$$t_s = \frac{\alpha}{\pi} \left[\frac{1 + x_s^2}{2} \ln \frac{X_s}{m_e^2} - x_s \right],$$

$$t_p = \frac{\alpha}{\pi} \left[\frac{1 + x_p^2}{2} \ln \frac{X_p}{m_e^2} - x_p \right],$$

where x_s and x_p are the fractions of energy lost by the incident electron and by the scattered electron, respectively,

$$x_s = \frac{E - \omega_s}{E},$$

$$x_p = \frac{E'}{E' + \omega_p}$$

and

$$X_s = 2(E - \omega_s)E'(1 - \cos \theta),$$

$$X_p = 2EE'(1 - \cos \theta).$$

According to [17], the energy cutoff for the elastic peak has been set in the implementation of the event generator to $\Delta E_r = 3 \cdot 10^{-3} E'_{el}(E, \theta)$, where $E'_{el}(E, \theta)$ is given by Equation (A.7).

5.3.3 Sampling function

For the elastic scattering, the energy straggling effect and the radiative corrections were treated together to obtain a sampling function for the variables t , E' and θ .

At any angle θ , the energy cutoffs ΔE_s and ΔE_r divide the (E, E') -plane into four regions according to:

$$\begin{array}{ll} \text{region I:} & E_0 > E > E_0 - \Delta E_s, \quad E'_{el}(E, \theta) > E' > E'_{el}(E, \theta) - \Delta E_r; \\ \text{region II:} & E < E_0 - \Delta E_s, \quad E'_{el}(E, \theta) > E' > E'_{el}(E, \theta) - \Delta E_r; \\ \text{region III:} & E_0 > E > E_0 - \Delta E_s, \quad E' < E'_{el}(E, \theta) - \Delta E_r; \\ \text{region IV:} & E < E_0 - \Delta E_s, \quad E' < E'_{el}(E, \theta) - \Delta E_r. \end{array}$$

Considering this subdivision, the distinction between peak events and tail events must be redefined. Only in the case of region I, the final energy E' is fixed once given the beam energy E_0 and the scattering angle θ . In the cases of regions II, III and IV, E' is not determined given E_0 and θ and must be sampled independently. For this reason only events coming from region I are

considered as peak events, while the rest of the events are referred to as tail events.

Integrating over the azimuthal angle ϕ , the peak events sampling function for t and θ is given by the differential cross section:

$$\frac{d\sigma_{el}^{peak}}{d\theta}(t, \theta) = \Delta\phi \sin\theta \cdot J_e^{\Delta E_s}(E_0, t) \cdot \left. \frac{d^2\sigma}{d\Omega} \right|_{peak}(E_0, \theta). \quad (5.11)$$

The total cross section for the elastic peak events is:

$$\sigma_{el}^{peak} = \int_0^T \frac{dt}{T} \int_{\theta_A}^{\theta_B} d\theta \frac{d\sigma_{el}^{peak}}{d\theta}(t, \theta) \simeq 0.21\text{nb}, \quad (5.12)$$

where the total length of the target is $T = 1.1 \cdot 10^{-2}$ radiation lengths.

Similarly, for the tail events, t , E' and θ are sampled from:

$$\begin{aligned} \frac{d^2\sigma_{el}^{tail}}{d\theta dE'}(t, \theta, E') = \Delta\phi \sin\theta \left[I_e(E_0, E, t) \cdot \left. \frac{d^2\sigma}{d\Omega} \right|_{peak}(E_{el}(E', \theta), \theta) \quad + \right. \\ \left. J_e^{\Delta E_s}(E_0, t) \cdot \left. \frac{d^3\sigma}{d\Omega dE'} \right|_{tail}(E_0, E', \theta) \quad + \right. \\ \left. \int_{E_{el}(E'_{low}, \theta)}^{E_0 - \Delta E_s} dE I_e(E_0, E, t) \cdot \left. \frac{d^3\sigma}{d\Omega dE'} \right|_{tail}(E, E', \theta) \right], \end{aligned} \quad (5.13)$$

where $E_{el}(E', \theta)$ is the inverse function of $E'_{el}(E, \theta)$ and the three terms in the square parenthesis represent the contributions of regions II, III, and IV, respectively. The total cross section for the elastic scattering tail events is:

$$\sigma_{el}^{tail} = \int_0^T \frac{dt}{T} \int_{\theta_A}^{\theta_B} d\theta \int_{E'_{low}}^{E'_{el}(E_0, \theta)} dE' \frac{d^2\sigma_{el}^{tail}}{d\theta dE'}(t, \theta, E') \simeq 0.18\text{nb}. \quad (5.14)$$

In conclusion, sampling one elastic event implies choosing whether the event belongs to the peak or to the tail. In the former case, t and θ are sampled from the function defined in Eq. (5.11) and E' is calculated consequently. In the latter case, the function defined in Eq. (5.13) is used to sample t , θ and E' . The peak events are chosen with a probability p_{peak} equal to:

$$p_{peak} = \frac{\sigma_{el}^{peak}}{\sigma_{el}^{peak} + \sigma_{el}^{tail}}, \quad (5.15)$$

the tail events with probability $p_{tail} = 1 - p_{peak}$.

5.4 Inelastic electron scattering off the proton

The electron-proton scattering is said to be inelastic, when it is accompanied by hadron production. The centre of mass energy W of the final hadronic state can

assume any real value above the pion production threshold $W_{th} = 1073$ MeV. This means that, for the inelastic scattering, there is one more independent kinematical variable as compared to the case of the elastic scattering without radiative corrections. The final electron energy E' is considered to be the independent variable together with the scattering angle θ . The relation between E' and W is given by Equation (A.8).

The inclusive differential cross section for a given electron kinematics, integrated over all possible hadronic final states, can be written with the formalism of virtual photon absorption [25, 28]. The cross section is separated into a kinematical factor Γ , representing the flux of virtual photons exchanged between electron and proton, and a dynamical part giving the total virtual photon-absorption cross section σ_{γ^*} of the proton:

$$\left. \frac{d^3\sigma}{d\Omega dE'} \right|_{inel}(E', \theta) = \Gamma \sigma_{\gamma^*}. \quad (5.16)$$

Defining ε as the ratio of longitudinal to transverse polarization of the virtual photons,

$$\varepsilon = \left[1 + 2 \frac{|\mathbf{q}|^2}{Q^2} \tan^2 \frac{\theta}{2} \right]^{-1}, \quad (5.17)$$

and k_γ as the laboratory energy needed by a real photon for exciting a hadronic system with centre of mass energy W ,

$$k_\gamma = \frac{W^2 - M_p^2}{2M_p}, \quad (5.18)$$

the factor Γ assumes the form:

$$\Gamma = \frac{\alpha}{2\pi^2} \frac{E'}{E} \frac{k_\gamma}{Q^2} \frac{1}{1 - \varepsilon}. \quad (5.19)$$

In the literature (e.g. [28]), the cross section σ_{γ^*} is expressed with explicit dependence on the kinematical variables W and Q^2 , rather than E' and θ . Additionally, it can be seen as the sum of two cross sections σ_T and σ_L , describing the absorption of transversely polarized and longitudinally polarized virtual photons, respectively:

$$\sigma_{\gamma^*}(W, Q^2) = \sigma_T(W, Q^2) + \varepsilon \sigma_L(W, Q^2). \quad (5.20)$$

The explicit form of σ_{γ^*} , hence of the sampling function for E' and θ in Equation 5.16, depends on the model used to describe the pion production through the two channels:

$$\begin{aligned} e^- + p &\rightarrow p + \pi^0, \\ e^- + p &\rightarrow n + \pi^+. \end{aligned}$$

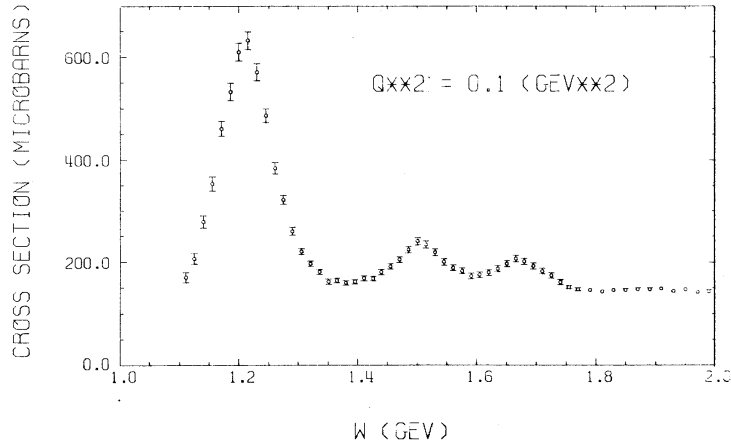


Figure 5.2: Virtual photon-absorption cross section as a function of W , with fixed $Q^2=0.1\text{GeV}^2$. Data are taken from Brasse et al. [30].

In this work, the unitary isobar model by Drechsel et al. [29] has been adopted. The implementation of the model, namely the program MAID has been used to calculate the cross sections σ_T and σ_L for the two given channels. Such model can well describe the data for W -values ranging from the pion threshold up to at least over the $\Delta(1232)$ resonance. This corresponds to about $1100\text{ MeV} < W < 1400\text{ MeV}$ with fixed $Q^2 = 0.1\text{ GeV}^2$, according to the data of Brasse et al. [30] shown in Figure 5.2. Looking at A4 experimental spectrum in Figure 3.2, this is also the interesting W -range for the simulation, though in that spectrum the value of Q^2 is not the same for different values of W . However the same W -range in the A4 spectrum corresponds to the Q^2 -range $(0.08, 0.18)\text{ GeV}^2$, which means that the kinematics of the data of Figure 5.2 and of the A4 spectrum are in first approximation comparable.

The total cross section for the inelastic scattering without considering straggling and radiative corrections is

$$\sigma_{inel} = \Delta\phi \int_{E'_{low}}^{E'_{up}} dE' \int_{\theta_A}^{\theta_B} d\theta \sin\theta \left. \frac{d^3\sigma}{d\Omega dE'} \right|_{inel}(E', \theta) \simeq 0.19\text{nb}, \quad (5.21)$$

with $E'_{low}=120\text{ MeV}$ and $E'_{up}=620\text{ MeV}$, since in the considered θ -interval the maximal E' corresponding to the pion threshold amounts to 616 MeV .

Finally, the position t of the scattering in the target is sampled from the uniform distribution in the range $(0, T)$.

5.5 Scattering off aluminium

Another background contribution to the spectrum, that must be taken into account, comes from the scattering of the beam electrons off the aluminium in the target input and output windows. The most relevant interactions between electrons and Al nuclei at these energies are the quasielastic scattering off the bound nucleons and their Δ -excitation.

For both processes there are two independent kinematical variables, namely E' and θ . Therefore, the differential cross section of the e -Al scattering has the form:

$$\frac{d^3\sigma}{d\Omega dE'} \Big|_{Al} (E', \theta) = \frac{d^3\sigma}{d\Omega dE'} \Big|_{quasiel} (E', \theta) + \frac{d^3\sigma}{d\Omega dE'} \Big|_{\Delta} (E', \theta). \quad (5.22)$$

To calculate these cross sections, a code based on a Fermi-gas nuclear model by Moniz [31] was used. The binding energy of the nucleons are calculated in a shell model, solving the Schrödinger equation with a Wood-Saxon well as central potential and a first derivative Wood-Saxon potential for the spin-orbit interaction².

The integration of Equation 5.22 gives the total cross section for the scattering off aluminium:

$$\sigma_{Al} = \Delta\phi \int_{E'_{low}}^{E'_{up}} dE' \int_{\theta_A}^{\theta_B} d\theta \sin\theta \frac{d^3\sigma}{d\Omega dE'} \Big|_{Al} (E', \theta) \simeq 16.25\text{nb}, \quad (5.23)$$

where $E'_{low}=120$ MeV. The quasielastic peak spreads up to energies E' higher than the elastic energy E'_{el} of the e - p scattering, because of the Fermi momenta of the nucleons. In order to include the whole quasielastic peak, the upper limit for the integration in E' was set to $E'_{up}=850$ MeV. The scattering position for the Al events coming from the input window and from the output window was set on the geometrical centre of the respective layer of aluminium. Such layers are situated at the extremities of the target. This implies that events with scattering angle θ lying outside the usual interval (33.6° , 36°) could contribute more frequently, on average, to the selected channel (see Section 5.1). Because of this, the sampling interval of θ , hence the integration interval in equation (5.23), was extended to $\theta_A=33^\circ$, $\theta_B=37^\circ$, to make sure that all events which are able to give a contribution to the chosen channel are included.

Like in the case of inelastic scattering off the proton, straggling effect and radiative corrections were not yet included.

²The calculation of the binding energies was performed by J. Van de Wiele, Institut de Physique Nucleaire Orsay, and privately communicated. The code for calculating the cross sections was implemented by M. El Yakoubi and J. Van de Wiele.

Chapter 6

Conclusions and outlook

In summary, the experimental apparatus of the A4 Collaboration has been described in Chapter 3. This apparatus is able to detect the beam electrons scattered off the liquid hydrogen target and to measure their energy. The number of detected electrons is histogrammed according to their energy, giving an experimental energy spectrum. A simulation of the detector response to the scattered electrons has been implemented and described in Chapter 4. An expected theoretical energy spectrum of these scattered electrons has been obtained implementing an event generator, which includes the most important scattering processes for the electrons. This event generator has been described in Chapter 5. In order to compare the theoretical energy spectrum of this event generator with the experimental energy spectrum, the simulation of the detector response has been applied to the generated events.

6.1 Result of the simulation, comparison with the experimental energy spectrum

Using the simulation of the detector response for tracking the primary electrons of the output events of the event generator, one obtains an energy spectrum, which can be compared with the experimental spectrum.

The events of the various processes have been simulated separately, so that the contribution of each process can be distinguished within the simulated spectrum. After simulating the detector response for all processes, one obtains one simulated histogram for each process. To have one histogram comparable with the histogram of the experimental spectrum, the histograms corresponding to all processes have to be rescaled with an appropriate factor and summed together.

For simplicity, the following general formalism can be applied. Considering k different processes X_i ($i = 1, \dots, k$), with their corresponding histograms H_i ,

the total simulated histogram H_S is:

$$H_S = \sum_{i=1}^k f_i H_i, \quad (6.1)$$

where f_i are the scaling factors for the respective processes X_i . Each one of these scaling factors is calculated as the ratio $f_i = E_i/S_i$, where S_i is the number of simulated events generated with kinematical variables within the selected ranges (see Section 5.1) according to the differential cross section of the process X_i . E_i is the expected number of electrons scattered within the same kinematical ranges according to the process X_i , during the run time t_R with a beam current I . The different processes have different total cross sections, in the sense defined in Chapter 5, and are associated with different “targets”, namely the liquid hydrogen volume, the aluminium input and output windows. These differ in length, density and mass of the particle responsible for the electron scattering, that is the proton and the aluminium nucleus, respectively. With σ_i the total cross section of the process X_i , and l_i , ρ_i and M_i the length, the density and the scatterer mass of the corresponding target, respectively. The expected number of electrons E_i for the process X_i is then:

$$E_i = \sigma_i \frac{\rho_i}{M_i} l_i I t_R. \quad (6.2)$$

After applying this rescaling and summation, the obtained simulated histogram H_S can be compared with the experimental energy spectrum like shown in Figure 6.1. It is important to stress, that the presented simulated energy spectrum is obtained exclusively from information about the experimental apparatus and about the physics of the electron scattering and of the passage of particles through the matter. No information from the experimental energy spectrum itself was used.

Looking at Figure 6.1, one notices a very good agreement between simulation and experiment in the energy range from the peak corresponding to the excitation of the $\Delta(1232)$ resonance, that is from the green peak at about channel 100, upwards. From channel 100 to channel 140, that means from the pion production threshold up to the maximum of the $\Delta(1232)$ resonance peak with increasing W (see also Figure 3.2), the agreement between simulated and experimental spectrum lies on the 13% level. In the low energy part of the spectrum, i.e. at the left side of the $\Delta(1232)$ resonance peak in Figure 6.1, the agreement becomes very bad, since the largest part of the experimental signal is not reproduced in the simulation.

From this observations, one can draw the following conclusions. The detailed simulation of the detector response described in Chapter 4 provides a reliable method for comparing the energy spectrum obtained in the experiment

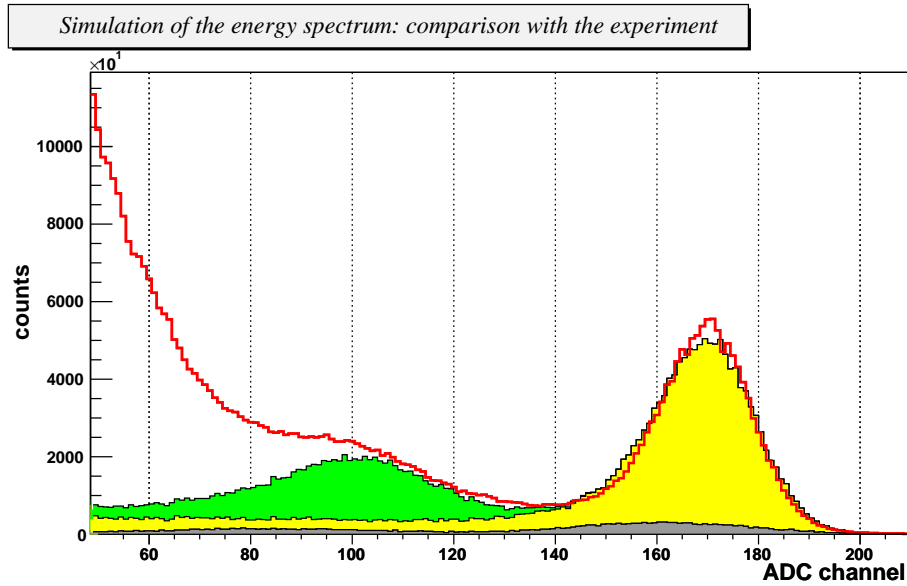


Figure 6.1: Comparison of the result of the simulation with the experimental energy spectrum. The red line corresponds to the experimental spectrum, it is the same as in Figure 3.2. The solid histogram is the result of the simulation presented in this work. Different colours differentiate the contributions of different processes. The upper profile of the solid histogram represents the sum of all contributions. The elastic scattering, taking into account straggling and radiative corrections, is shown in yellow. The elastic peak appears on the right and the radiative tail spreads to lower energy on the left side, contributing also to the energy region of the $\Delta(1232)$ resonance (between about channel 80 and channel 120). The inelastic scattering is shown in green, reproducing about the channel 100 the structure due to the excitation of the $\Delta(1232)$ resonance. The contributions of the input and output aluminium windows produce the thin layer of background shown in gray at the bottom of the picture.

with the scattering processes that are theoretically expected to occur in the target. In other words, since the energy spectrum of the experiment can be reproduced so well in the higher energy range, only using information coming from the physics and the experimental specifications, one can persuade oneself that the detector response is well reproduced in the whole energy range.

If the simulation of the detector response is assumed to be reliable, a second conclusion becomes necessary when looking at the left side of Figure 6.1. The huge discrepancy between the experimental and the simulated histogram at the lower energy range must be due to some physical process, which was not taken into account in the event generator. Possibly the signal in the detector can be produced by other particles than electrons, like photons, pions or protons which are produced in the experiment but not considered in the simulation. This issue is one of the main subjects of the future work and is briefly discussed in the next section.

The last conclusion concerns the measurement of the parity violating helicity asymmetry in the excitation of the $\Delta(1232)$ resonance. With the present knowledge of the inelastic part of the energy spectrum, i.e. with the understanding of the contributions to the spectrum in the W range from the pion production threshold up to the maximum of the $\Delta(1232)$ resonance peak evinced by the result of the simulation (Figure 6.1), in principle, the extraction and the analysis of the helicity asymmetry for that W range can be already worked out and the result of the analysis compared with the theoretical predictions.

6.2 Outlook

There are two main guidelines for proceeding with the present work. On the one hand, it is necessary to start working on the analysis of the helicity asymmetry in the excitation of the $\Delta(1232)$ resonance. This issue is very similar to what was already done within the A4 collaboration for the helicity asymmetry in the elastic electron-proton scattering. Indeed, the value of the asymmetry for the energy range corresponding to the $\Delta(1232)$ excitation can already be extracted. The most relevant difficulty would be the theoretical estimation of the dilution factor due to the background.

On the other hand, it is essential to work further on the simulation of the experiment, in order to extend the energy range of understanding of the energy spectrum to include the whole $\Delta(1232)$ resonance peak. About this last issue, several effects can be investigated. Four of them are cited in the following.

- The radiative tail from the elastic peak has been estimated in the peaking approximation, where it is assumed, that all hard photons radiated by internal bremsstrahlung are emitted with a momentum direction parallel

to the momentum either of the incoming electron or of the scattered electron. This is not true when the final electron energy is less than about one half of the energy of elastically scattered electrons with the same scattering angle [23]. One first consequence is that the radiative tail cross section for electrons with these final energies could be larger. The second consequence is that some photons, emitted by the scattering of electrons with other scattering angles, could hit the detector and have sufficient energy to contribute to the lower part of the energy spectrum of Figure 6.1¹.

- The pions produced by electrons scattering inelastically with any scattering angle can give contributions to the low energy part of the spectrum in two ways. The π^0 's decay still inside the target into two photons, which can reach the detector. This process was already considered in [17] but only photons with energy larger than 400 MeV were taken into account. The π^+ 's can either reach the detector themselves and contributing to the spectrum or decay according to $\pi^+ \rightarrow \mu^+ \nu_\mu$, in which case the μ^+ could hit the detector. For considering these last processes, the detector response to pions and muons remains still to be investigated.
- Multiple scattering processes, e.g. the double “Møller-Mott” scattering, have been already studied but could deserve a more systematic scrutiny. According to the results of [32], the contributions expected from these kind of processes should not be relevant.
- The last, minor aspect to be addressed concerns the radiative corrections and the straggling effect in the inelastic scattering off the proton and in the scattering off aluminium. Some calculations of the radiative corrections to the electron-proton inelastic scattering have been already performed, indicating that the effect to be expected from these corrections is not very large.

¹The response of the detector to photons with energies comparable with the electron energies has not been treated in this work. Though, some simulations have been undertaken and the detector response to the photons was found to be almost the same as the response to electrons of the same energy. There is, therefore, no possibility to distinguish between electrons and photons, like already stated in [17, 26].

Appendix A

Kinematics

The most general kinematics of inclusive electron proton scattering is known when the three four momenta k , k' and P are given. k and P are the four momenta in the initial state of electron and proton respectively. k' is the four momentum of the electron in the final state. The four momentum P' of the final hadronic state follows from the energy-momentum conservation law:

$$P' = P + k - k' = P + q, \quad (\text{A.1})$$

where the four momentum transfer q has been defined as:

$$q = k - k'. \quad (\text{A.2})$$

This is depicted schematically in Figure A.1. It shows the tree level Feynman graph corresponding to the electron proton scattering amplitude in the one photon exchange approximation, that is the four momentum transfer q is carried by a single virtual photon.

The components of the four momenta in the laboratory system be¹:

$$\begin{aligned} k &= (E, \mathbf{k}), \\ k' &= (E', \mathbf{k}'), \\ P &= (M_p, \mathbf{0}), \\ q &= (\omega, \mathbf{q}), \end{aligned} \quad (\text{A.3})$$

where M_p is the rest mass of the proton.

Considering the case of highly relativistic electrons both in the initial and final state, i.e. $k^2 = k'^2 = 0$, and being θ the angle between \mathbf{k} and \mathbf{k}' , one has:

$$\mathbf{k} \cdot \mathbf{k}' = EE' \cos \theta. \quad (\text{A.4})$$

Using (A.4) with (A.3), it is possible to express the positive squared momentum transfer Q^2 as a function of the kinematical variables in the laboratory frame²,

¹The speed of light is supposed to be $c=1$.

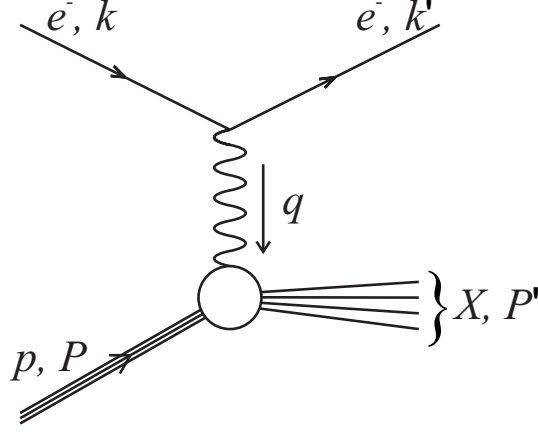


Figure A.1: One photon exchange Feynman diagram for the electron proton scattering amplitude.

$$Q^2 = -q^2 = 2EE'(1 - \cos \theta) = 4EE' \sin^2 \frac{\theta}{2}. \quad (\text{A.5})$$

Furthermore it is useful to have an expression for the hadronic final state invariant mass W . This can be obtained by squaring (A.1) and applying the definitions (A.3):

$$W^2 = P'^2 = M_p^2 - Q^2 + 2M_p\omega. \quad (\text{A.6})$$

Elastic scattering. Figure A.1 shows the most general final state for the electron proton scattering process. Considering a proton in the final state instead of the general hadronic state X , one would have the elastic scattering case. In such a case, the invariant mass W would be equal to the mass of the proton M_p . Substituting $W=M_p$ in (A.6) and combining this with (A.5), one obtains an expression for E' in terms of θ , which becomes the only independent kinematical variable:

$$E' = \frac{E}{1 + \frac{2E}{M_p} \sin^2 \frac{\theta}{2}}. \quad (\text{A.7})$$

Inelastic scattering. In case the final state X were not a proton, it could include more than one particle, e.g. produced by the decay of an excited state. Still, it is possible to know the invariant mass W of such a state, which is the energy in the centre of mass system of initial proton and virtual photon (Figure A.1). For instance, at the maximum of the $\Delta(1232)$ peak one has $W = 1.232\text{GeV}$. If W is considered as a new independent variable together

²The convention used for the Lorentz metric tensor $g^{\mu\nu}$ ($\mu, \nu = 0, 1, 2, 3$) is $g^{\mu\nu} = \text{diag}(1, -1, -1, -1)$.

with the scattering angle θ of the electron, the combination of (A.6) with (A.5) gives:

$$E' = \frac{M_p^2 + 2M_p E - W^2}{2M_p + 4E \sin^2 \frac{\theta}{2}} . \quad (\text{A.8})$$

Equation (A.8) allows calculating the final energy E' of an electron scattered with polar angle θ in the laboratory system having excited one hadronic state with invariant mass W . In other words, referring to Section 3.1.1, the expression says which part of the electron energy spectrum, at a given angle θ , corresponds to a given invariant mass W .

Appendix B

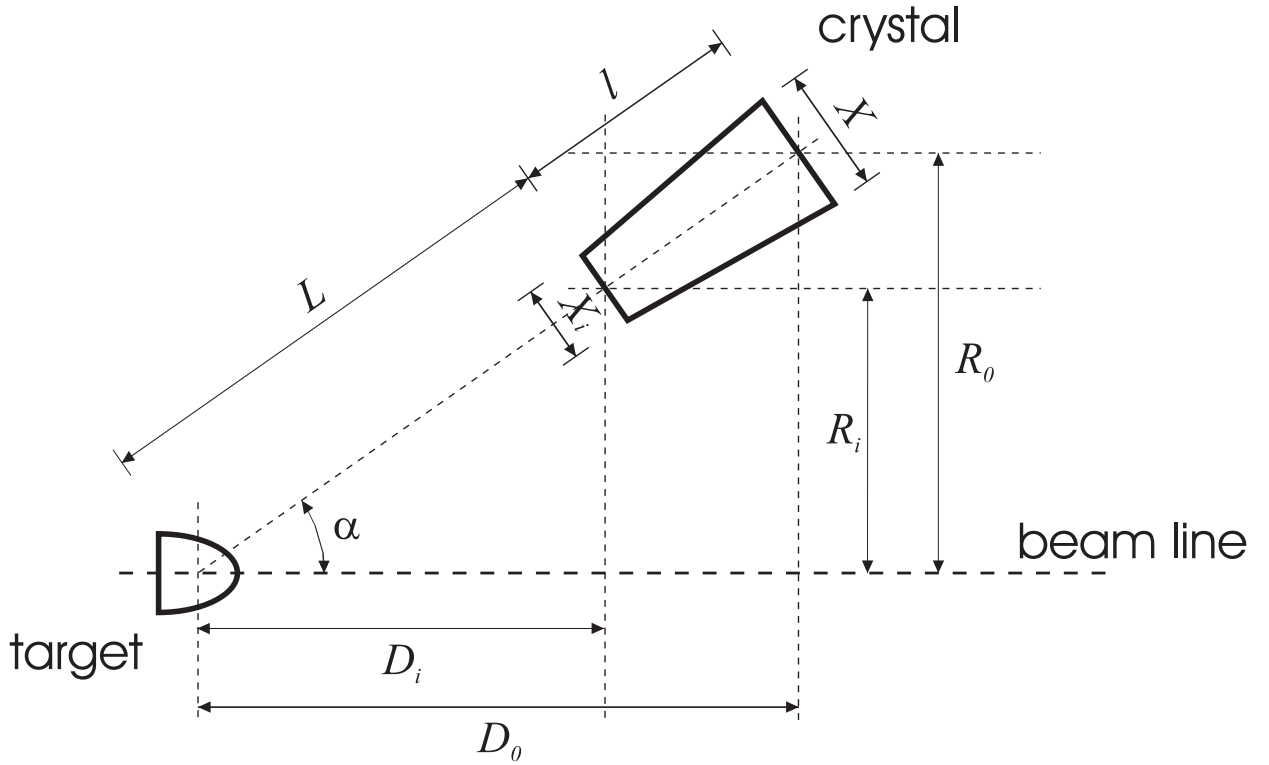
Geometry details

Table B.1: Position and orientation of crystals. See Figure B.1 - (a) for definitions

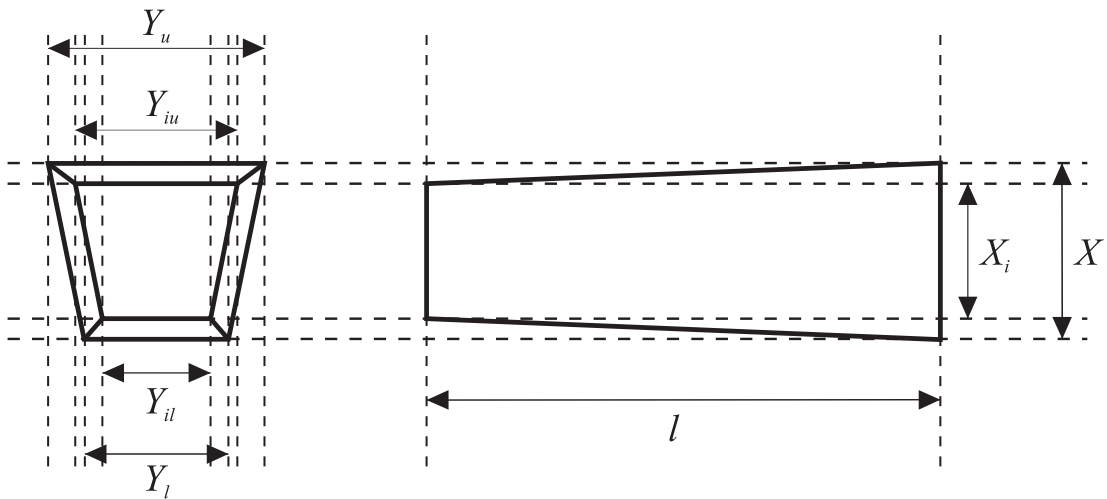
ring no.	α ($^\circ$)	D_i (mm)	D_0 (mm)	R_i (mm)	R_0 (mm)	L (mm)
1	39.22	737.8	854.0	602.1	697.0	952.3
2	37.69	779.5	902.2	602.1	697.0	984.9
3	36.20	822.6	952.1	602.1	697.0	1019.4
4	34.77	867.2	1003.8	602.1	697.0	1055.8
5	33.39	913.5	1057.4	602.1	697.0	1094.1
6	32.06	961.4	1112.9	602.1	697.0	1134.4
7	30.77	1011.2	1170.5	602.1	697.0	1176.9

Table B.2: Dimensions of crystals. See Figure B.1 - (b) for definitions

ring no.	l (mm)	X_i (mm)	X (mm)	Y_{il} (mm)	Y_l (mm)	Y_{iu} (mm)	Y_u (mm)
1	150.0	25.9	30.0	25.5	29.5	26.4	30.5
2	155.1	25.9	30.0	25.5	29.5	26.4	30.5
3	160.6	25.9	30.0	25.5	29.5	26.4	30.5
4	166.3	25.9	30.0	25.5	29.5	26.4	30.5
5	172.3	25.9	30.0	25.5	29.5	26.4	30.5
6	178.7	25.9	30.0	25.4	29.5	26.4	30.5
7	185.4	25.9	30.0	25.4	29.4	26.4	30.6



(a)



(b)

Figure B.1: (a) - Definition of the direction and position parameters of crystals. (b) - Definition of the dimensions of crystals

Bibliography

- [1] D.v. Harrach, MAMI proposal A4/1-93, MAMI, Mainz, 1993
- [2] F.E. Maas et al., Phys. Rev. Lett. 93, 022002 (2004)
- [3] F.E. Maas et al., nucl-ex/0410013 (2004)
- [4] L.M. Nath, K. Schilcher, M. Kretzschmar, Phys. Rev. D 25, 9 (1982) 2300-2305
- [5] H.W. Hammer, D. Drechsel, Z. Phys. A 353 (1995) 321-331
- [6] N.C. Mukhopadhyay, M.J. Ramsey-Musolf, S.J Pollock, J. Liu, H.-W. Hammer, Nucl.Phys. A633 (1998) 481-518
- [7] R.N. Cahn, F.J. Gilman, Phys. Rev. D 17, 5 (1978) 1313-1322
- [8] Y. Imai, *Entwicklung eines optischen Systems für ein Compton-Rückstreupolarimeter*, Diploma thesis, Mainz, 2003
- [9] J. Diefenbach, *Aufbau einer elektronischen Stabilisierung für das A4-Compton-Polarimeter*, Diploma thesis, Mainz, 2003
- [10] C. Weinrich, *Entwicklung eines Transmissions-Compton-Polarimeters für das A4-Experiment*, Diploma thesis, Mainz, 2000
- [11] T. Hammel, *Luminositätsmessung und Korrektur helizitätskorrelierter Effekte für ein Experiment zur Messung der Paritätsverletzung in der elastischen Elektronenstreuung*, Doctoral thesis, Mainz, 2003
- [12] K. Grimm, *Aufbau eines Lichtauslesesystems für ein Bleifluorid-Kalorimeter zur Messung der Paritätsverletzung in der elastischen Elektronenstreuung*, Doctoral thesis, Mainz, 2002
- [13] P. Achenbach et al., Nucl. Instr. and Meth. A416 (1998) 357-363.
- [14] D. F. Anderson, M. Kobayashi, C. L. Woody and Y. Yoshimura, Nucl. Instr. and Meth. A290 (1990) 385-389.

- [15] P. Achenbach, *Aufbau eines Bleifluorid-Kalorimeters zur Messung der Paritätsverletzung in der elastischen Elektronenstreuung*, Doctoral thesis, Mainz, 2001
- [16] Photonis, *Photomultiplier tubes*, Product specifications booklet, 2000
- [17] B. Collin, *Contenu étrange du nucléon: mesure de l'asymétrie de violation de parité dans l'expérience PVA4 à MAMI*, Doctoral thesis, Orsay, 2002
- [18] G. Folger, S. Giani, *Introduction to Geant4*, Geant4 online User's documentation. <http://wwwasd.web.cern.ch>
- [19] H-P. Wellisch, M. Maire, L. Urban, *Physics Reference Manual*, Geant4 online User's documentation. <http://wwwasd.web.cern.ch>
- [20] D.H. Wright et al., *User's Guide: For Application Developers*, Geant4 online User's documentation. <http://wwwasd.web.cern.ch>
- [21] A. Levin, C. Moisan, *A More Physical Approach to Model the Surface Treatment of Scintillation Counters and its Implementation into DETECT*, TRIUMF Preprint TRI-PP-96-64, Oct. 1996
- [22] S. Eidelman et al., *Phys. Lett. B* 592, 1 (2004)
- [23] L. W. Mo and Y. S. Tsai, *Rev. Mod. Phys.* 41, 205 (1969)
- [24] B. Povh, K. Rith, C. Scholz, F. Zetsche, *Teilchen und Kerne*, Springer-Verlag, 1993
- [25] A. W. Thomas, W. Weise, *The structure of the nucleon*, Wiley-VCH, 2001
- [26] S. Ong, M. P. Rekalo, J. Van de Wiele, *Eur. Phys. J. A* 6, 215-223, 1999
- [27] Y. S. Tsai, *Phys. Rev.* 122, 6 (1961) 1898-1907
- [28] D. Drechsel, L. Tiator, *J. Phys. G: Nucl. Part. Phys.* 18, 449-497, 1992
- [29] D. Drechsel, S.S. Kamalov, L. Tiator, *Nucl. Phys. A* 645 (1999) 145-174
- [30] Brasse, F. W., W. Flanger, J. Gyler, S. P. Goel, R. Haidan, M. Merkwitz, and H. Wriedt, 1976, *Nucl. Phys. B* 110, 413
- [31] E.J. Moniz, *Phys. Rev.* 148, 4 (1969) 1154-1161
- [32] E. Heinen-Konschak, *Vorbereitende experimentelle Studien für die Messung der Paritätsverletzung in der elastischen ep-Streuung*, Doctoral thesis, Mainz, 1994

List of Figures

3.1	Principle of the A4 experiment	11
3.2	Example of an energy spectrum.	13
3.3	Details of the experimental concept.	15
3.4	Side view of the liquid hydrogen target (dimensions in mm). . .	17
3.5	Side view of the vacuum scattering chamber (dimensions in mm). 18	
3.6	Schematic view of one frame supporting 7 crystals with their photomultipliers	19
3.7	Schematic view of the lead fluoride Cherenkov calorimeter . . .	20
3.8	Refractive index n of PbF_2 as a function of the wavelength λ . . .	22
3.9	Spectral sensitivity characteristic of some Photomultipliers. . .	24
3.10	Representation of the readout scheme of the detector.	27
4.1	Geometrical setup of the simulation, GEANT4 graphical output view	34
4.2	Absorption length of PbF_2	38
4.3	Simulated spectral response of the photomultipliers	39
4.4	Number of photoelectrons in one phototube as a function of the deposited energy in the correspondent crystal.	41
4.5	Statistical frequencies of the number of photoelectrons for dif- ferent values of the deposited energy E_{dep}	43
4.6	Sample estimation of σ_{ph}^2 as a function of the deposited Energy. 46	
5.1	Feynman diagrams for calculating the radiative corrections on the elastic electron-proton scattering	55
5.2	Virtual photon-absorption cross section as a function of W . . .	59
6.1	Comparison of the result of the simulation with the experimen- tal energy spectrum.	63
A.1	One photon exchange Feynman diagram for the electron proton scattering amplitude.	68
B.1	(a) - Definition of the direction and position parameters of crys- tals. (b) - Definition of the dimensions of crystals	72

Acknowledgments

At this point, I would like to dedicate a page for thanking all the people who helped me and collaborated with me in realizing this work. Although it would be somehow difficult to cite really everyone who contributed more or less directly, my acknowledgment is meant to be directed to all of them. Here I will just remember those persons who have been most closely involved in the activity.

Prof. v. Harrach gave me the opportunity to take part to the A4 experiment, an experience which I found very interesting and instructive for the study of the physics. He has been helpful, ready to discuss and gave me useful advice, when I was in the need of it.

Dr. Frank Maas has followed every step of this work, supervising me and explaining me with much patience details related with lots of topics, concerning this experiment but also concerning the experimental physics in general. His always friendly support has been essential for this work, like his many suggestions as I was writing it.

Jürgen Diefenbach and Yoshio Imai have helped me directly in writing this work, by reading it and giving me very fruitful comments. Beyond the issue of writing, they have been always ready to help me every time I had whatsoever difficulty.

Jeong Han Lee and Christoph Weinrich has been also, at every time, ready to solve any kind of problem for me. Jeong Han provided also very useful material about the target.

Ernst Schilling gave me more useful information about the target.

Sebastian Baunack was very helpful explaining me many details of the experiment, in particular about the data analysis. The discussions with him were always interesting, also beyond the concern of the physics.

Thorsten Hammel has been very patient with me, when I was asking questions. Boris Gläser is always ready for explaining technical topics, which are often amazing for me and which I find very enlightening.

Simon Taylor has been many times the right man, in the right place, at the right time. I received really many useful suggestions and ideas from him. Particularly I appreciate his enthusiasm for the physics, which I admire.

Riad Suleiman is for me as much admirable, and not only for the physical

knowledges. In this field, however, he demonstrated very good capability in matching the understandings of theory and of experiment and in being able to explain them.

Jacques Van de Wiele is also endowed with these capabilities. He has to be thanked for the largest part of my understanding of the theoretical aspects related with this work.

José Fernando Ortega Sánchez should maybe occupy the first place in this list. Without him, I would have never come to Mainz.

Finally, I would like to thank my family, my mother, my sister and my brother, for giving me their approval in doing what I do... or being what I am.

I leave the last place to the person who is most close to me now. Alicia in the last years has been my family here in Mainz.

Hiermit erkläre ich, daß ich die vorliegende Arbeit selbständig verfaßt und keine anderen, als die angegebenen Quellen und Hilfsmittel verwendet habe.

Mainz, den 26. Oktober 2004

Luigi Capozza